Master of Science Thesis VT20

Rebecka Ericsson Szecsenyi

Characterization of Radiomics Features Extracted from Images Generated by the 0.35 T Scanner of an Integrated MRI-Linac

Main supervisor:
Eduardo G. Moros
Moffitt Cancer Center
Tampa, Florida

Co-supervisor:
Crister Ceberg
Lund University

Department of Medical Radiation Physics,
Clinical Sciences, Lund, Lund University

Populärvetenskaplig sammanfattning

Cancer är en vanlig sjukdom i dagens samhälle, och man estimerar att en av tre i Sverige någon gång i livet kommer få en cancerdiagnos. De stora framsteg som skett inom forskning och teknologi har gjort att man har blivit bättre på att behandla så att allt fler överlever sin sjukdom. Det finns dock studier som tyder på att personer med samma diagnos kan reagera olika på samma typ av behandling. Varje tumör och patient är unik i sin genuppsättning och inom onkologi strävar man därför efter att ge en så individualiserad behandling som möjligt. Olika former av medicinsk bilddiagnostik (röntgen, magnetresonanstomografi (MR), Datortomografi (DT) m.m.) används idag inom sjukvården som ett verktyg för att säkerställa diagnos, rita ut tumör/omgivande organ, dosplanera o.s.v. så att behandlingen kan skräddarsys så mycket som möjligt. Bilderna granskas visuellt av specialiserade läkare som bedömer tumörens utbredning, form och lokalisation. Detta kallas för en kvalitativ bedömning.

Radiomics är ett relativt nytt forskningsområde som innebär att man studerar medicinska bilder kvantitativt, d.v.s. information i bilden kan översättas till en faktiskt siffra, s.k. *features*, som kan kopplas till en specifik frågeställning. Den underliggande hypotesen är att medicinska bilder inte enbart kan tolkas visuellt, utan att de består av data som kan ge ytterligare diagnostiskt värde. Heterogena strukturer och mönster ej synliga för blotta ögat tros innehålla biologisk/fysiologisk information om tumören eller omgivande vävnad som kan användas för att optimera behandlingen efter patientens behov. Det långsiktiga målet med radiomics är att undersöka dessa kvantitativa features för ett stort antal patienter och på så vis kunna bygga kliniska modeller som kan användas för att förbättra diagnostik och beslutstagande.

Målet med detta examensarbete var att undersöka ett stort antal radiomic features som beräknats från bilder tagna med en s.k. integrerad MR-Linac. Det finns flera yttre faktorer utöver biologiska/fysiologiska förändringar som kan påverka resultatet av en features värde såsom bildtagningsmetod, inställningar, upplösning o.s.v.. Man måste således säkerställa vilka features som är stabilia under olika förhållanden så att ett kvantitativt mått beror på fysiologi och inte olika bildinställningar. I detta arbete undersöktes därför stabiliteten av features från både patient- och fantomdata (fantom är solida objekt som används för kvalitetskontroll av utrustning) med olika inställningar. Ett flertal gemensamma stabila features identifierades och ett stort antal av dessa har även visat sig vara kopplade till kliniskt utfall i literaturstudier. Detta är lovande då radiomics har förutsättningarna att spela en stor roll i individanpassad onkologi.

Abstract

Purpose: In an era of personalized oncology where the aim is to give every patient the right treatment at the right time an area of promising research is emerging called radiomics, or quantitative image analysis. The main underlying hypothesis is that pathophysiological information can be found in image texture not visible to the bare eye that can improve diagnosis, treatment adaption or be linked to a certain clinical outcome. *This project investigates the stability and repeatability of radiomic features extracted from images acquired with an integrated MRI-Linac with a 0.35 T scanner.* The main objective was to identify radiomic features that are robust over various imaging conditions in both phantom and human data.

Methods: *The patient dataset included 50 images from ten stereotactic body radiation therapy (SBRT) pancreas cancer patients treated with 5 fractions, given on a daily basis, on the integrated MRI-Linac.* Two anatomical sites were selected to represent heterogeneous invariant tissue: the kidneys and liver. Eleven images from a Magphan RT phantom and 11 images from a ViewRay Daily QA phantom acquired monthly and daily respectively, constituted the basis for the phantom data, representing ideal imaging conditions. All images were acquired with a True Fast Imaging with Steady State Free Precession (TRUFI) pulse sequence with two different protocols. A high resolution ($1.5mm^3$ voxel resolution) protocol was used for all phantom images and a protocol with lower resolution ($1.5mm^2$ x 3.0mm) was used to collect the patient images. Totally 1087 shaped-based, first order statistics, second order statistics and higher order statistical radiomic features were extracted from each region of interest (ROI) and subject. Stability was assessed with the Coefficient of Variation (CoV) where features with CoV<5% were classified as robust. Common robust features among all datasets were identified as a final step.

Results: There were in total 130 radiomic features demonstrating robustness (CoV<5%) among all datasets. Robust features could be identified within each category, apart from two second order statistics groups: Gray level size zone and Neighborhood gray tone difference. The mean value of the CoV and the corresponding standard deviation was calculated for each robust feature in all four datasets.

Discussion and Conclusion: Several robust features in common with the result of this work can be identified in other MRI-based radiomics studies, which is promising. However, no overall agreement is found between all studies, emphasizing the need of more stability assessment research. The result in this work indicates that robust radiomic features over various imaging conditions, in both phantom and patient data, can be identified. *It implies that phantom measurements can be used in stability assessment studies and that the 0.35 T scanner of the integrated MRI-Linac in this work is sufficiently stable over time for radiomic studies.* An additional promising finding is that many robust features also have been reported to have predictive value or discriminative power in other studies. Although preliminary, this result can serve as guidelines for further model building or further

radiomics studies.

Contents

ABBREVIATIONS

cCR = Clinical Complete Response
CoV = Coefficient of Variation
CT = Computed Tomography
DICOM = Digital Imaging and Communications in Medicine
FFF = Flattening-filter-free
GLCM = Gray Level Co-occurrence Matrix
GLRLM = Gray Level Run Length Matrix
GLSZM = Gray Level Size Zone Matrix
IBSI = Image Biomarker Standardization Initiative
ICC = Intraclass Correlation Coefficient
IGRT = Image Guided Radiation Therapy
IMRT = Intensity Modulated Radiation Therapy
LoG = Laplacian of Gaussian
LRE = Long Run Emphasis
MRI = Magnetic Resonance Imaging
NEX = Number of Excitations
NGTDM = Neighborhood Gray Tone Difference Matrix
OAR = Organ at Risk
OS = Overall Survival
PET = Positron Emission Tomography
QA = Quality Assurance
RF = Radio Frequency
RLNU = Run Length Non-Uniformity
ROI = Region of Interest
RPC = Run Percentage
RT = Radiation Therapy
SBRT = Stereotactic Body Radiation Therapy
SNR = Signal-to-noise Ratio
SRE = Short Run Emphasis
TRUFI = True fast and Steady State Precession

1 INTRODUCTION

One out of three people in Sweden will receive a cancer diagnosis at some time in their lives. Thanks to efforts in research and considerable technological advances two out of three will survive the disease [1]. Treatment method varies depending on type or stage of cancer, but it has been shown that people with the same diagnosis can respond differently to the same treatment. This entails for an emerging era within oncology called *precision medicine* or *personalized medicine*, meaning that treatment is tailored to each patient's tumor genetics [2] [3]. Medical imaging is an existing tool in radiation therapy for tumor staging, outlining, treatment planning, dose adaptation etc so that treatment can be as personalized as possible for every person. As a result from technological evolution an integrated system called MRI-Linac has been developed, which improves medical imaging even further. The system provides high soft tissue contrast images that are acquired in the planning stage or during actual treatment [4] [5]. Medical images are currently qualitatively analyzed by radiologists to state diagnosis. However, quantitative image analysis, *Radiomics*, is a promising area of research which aims to extract further pathophysiological information from tumors. By interpreting images not only as pictures but as data, the hypothesis is that texture not visible to the naked eye contain additional biological/physiological information, that can lead to treatment optimization [6] [7]. Hence, radiomics is an area of great promise in the pursuit of personalized medicine.

2 AIM

This master's thesis aims to investigate radiomic features extracted from images acquired with a 0.35 T scanner on an integrated MRI-Linac, with the primarily focus on stability, repeatability and reproducibility of the system. The main objective was to identify radiomic features that are robust across many imaging conditions in both phantom and patient images.

3 THEORETICAL BACKGROUND

3.1 Technical design and description of the ViewRay MRIdian system

The ViewRay MRIdian Linac (ViewRay Inc., Oakwood, USA) is a hybrid system combining a magnetic resonance imaging (MRI) system with a radiation therapy (RT) device. The MRI modality provides a superior soft tissue contrast in comparison to x-ray based methods, as well as the advantage that image acquisition is performed with no use of ionizing radiation [5]. *Image guided radiation therapy (IGRT) using techniques such as onboard cone-beam CT (CBCT) has already improved the accuracy of today's radiation therapy treatments, and is even further expanded through the actualization of the ViewRay integrated MRI-linac and thereof, MR-IGRT* [8].

This hybrid system consists of a 0.35 T split-bore superconducting magnet integrated with a 6 MV flattening-filter-free (FFF) linear accelerator, so that the two components share the same isocenter [4]. It has a 50 cm diameter spherical field of view and uses a 75 cm whole-body radio frequency (RF) transmit coil with integrated RF shielding. Furthermore, the gradient system has a maximum strength of 18 mT/m and a maximum slew rate of 200 T/m/s on each axis [9]. The system allows for 3D conformal RT and step-and-shoot intensity-modulated-radiation-therapy (IMRT) treatment plans [4].

The MRI system enables imaging pre- and post-treatment as well as cine imaging (in the sagittal plane at four frames/s) during the actual treatment. Both the daily set-up and the cine imaging are acquired with a True fast and Steady State Precession (TRUFI) pulse sequence which results in a T2/T1-weighted contrast [4]. Daily images are acquired to ensure accurate patient positioning, target localization and visualization of organs at risk (OAR). Additionally, online adaption of treatment plans is possible so that the dose distribution from the original plan is compared to the daily dose prediction, and can thereby be optimized depending on the daily anatomy [5] [4]. The cine MRI allows the user to contour a region of interest (ROI) around the target in the daily set-up image, used for online tracking and automatic beam control. A desired boundary is then defined which specifies a certain percentage of the target volume that is allowed to exceed the chosen boundary before the beam is interrupted [8].

3.2 Radiomics: Background and process

Medical imaging is a fundamental part of current diagnostics where modern techniques such as computed tomography (CT), positron emission tomography (PET)

and MRI are available. These modalities are widely used within oncology as standard practice for e.g. screening, staging or decision making where images are analyzed qualitatively by radiologists [10]. The aim of radiomics is to, in addition to a solely visual interpretation, extract more underlying information from the image not observable by the bare eye. There is an underlying hypothesis that texture, patterns, voxel value distribution and so on contain physiological information of diagnostic value [7]. By converting medical images into mineable data this information can be extracted mathematically to generate so-called quantitative imaging *features*. A large amount of possible imaging features exist, which will be discussed in further detail later on, that can be utilized to improve or support decision making [6] [11]. The idea is that this data, in combination with other patient information, eventually will constitute a basis for building descriptive models of patient response, outcome, treatment alternatives and so on [6]. Thus, by combining qualitative and quantitative information radiomics holds promise to play an important role within the future aspects of personalized oncology, i.e. precision medicine [12] [13] [14].

The work-flow of radiomics involves several steps; (i) image acquisition, (ii) identifying and segmenting volumes of interest, (iii) feature extraction, (iv) statistical analysis and (v) building predictive models [6] [11] [13]. Every step has challenges which will be described in more detail in the subsequent sections.

3.2.1 (i) Image acquisition

Radiomics can be performed on clinical MRI, PET or CT images to extract a large number of quantitative features [12]. However, for each modality there is also a great variation of imaging parameters and reconstruction methods which have been shown to influence the feature extraction outcome [14] [11]. In MRI differences regarding gradient strength, pulse sequence, acquisition protocols, k-space trajectory sampling etc will affect the outcome and reliability of the radiomic data [15]. This makes comparison between institutions difficult and urges the investigation of robust features, as well as standardized imaging protocols for radiomics to become a useful qualitative tool in the clinic [13] [6] [14].

3.2.2 (ii) Identifying and segmenting volumes of interest

A fundamental part of the physicians job is to study diagnostic medical images and based on location, size, geometry etc identify the region of interest [15]. Segmentation can then be done manually, automatically or semi-automatically which consequently will affect the final outcome of the evaluated imaging features [13]. This is therefore a critical and challenging step in the radiomics procedure. Manual segmentation is often considered as ground truth but is time consuming and affected by interreader variations [11]. Automatic and semi-automatic methods, such

as thresholding, region growing, artificial neural networks and so on [15], could offer a more rapid segmentation process [11]. However, due to challenges regarding areas with complex anatomy, reproducibility and reliability of the algorithm should be taken into consideration [6].

3.2.3 (iii) Feature extraction

Once segmentation is completed quantitative imaging features are extracted from the outlined volumes of interest. Medical images are commonly visually interpreted by radiologists by studying tumor shape, location, geometry, size or tissue contrast. The aim of radiomics is to provide further information, hidden within the feature data, in addition to these qualitative characteristics [16] [12]. However, different institutions use different software to extract features which will affect the outcome of the quantitative values. There is today no standard method for feature computation, but a large research collaboration called the Image Biomarker Standardization Initiative (IBSI) is working on implementing standard procedures and guidelines [17].

3.2.4 (iv) Statistical analysis

Depending on the study's purpose and setup, relating to e.g. clinical outcome, different statistical methods are suitable for handling the large number of radiomic features which, from a single image, can exceed hundreds or even thousands. Hence, there must be a systematic feature selection procedure to reduce the number of features [7] [11]. One approach to avoid overfitting of data is clustering, i.e. highly correlated features are identified and then collapsed into one descriptive feature. Another reduction method is based on the reproducibility of the feature values, using test-retest data [6] [12]. Once feature dimensionality have been reduced the most informative features can be identified and further analyzed for how they relate to e.g. treatment outcome [7].

As radiomics aim to provide additional information related to clinical outcome and decision support [6] it is essential that feature values are stable under various imaging conditions [18]. A model based on non-robust features might be unreliable when used to predict outcome on new data, hence emphasizing the importance of assessing feature robustness so that these models eventually can be implemented clinically [19]. However, there is at this moment no standardized guidelines on how to assess robustness, although it is recommended by IBSI as a prior step before feature selection [18].

Test-retest imaging, i.e. the same object or ROI is imaged twice within a certain time interval so that two similar images (however, not identical) are obtained, is a recommended method for stability assessment. Comparison between the two images

will allow for identification of non-robust features [19]. The Intraclass Correlation Coefficient (ICC) is a descriptive statistic, used in several studies [19] [18] [20] to quantify robustness in a test-retest setup. ICC describes the degree of correlation as well as agreement between measurements, and has different forms of calculation depending on the type of study [21]. Another similar descriptive statistic mentioned in literature [22] [23] [20] for studying variability and assess robustness, when e.g. looking at intrascanner variability, is the Coefficient of Variation (CoV) defined as:

$$CoV = 100 \cdot \frac{\sigma}{|\mu|} \tag{1}$$

were σ is the standard deviation and $|\mu|$ is the absolute value of the mean. It is expressed as a percentage and describes the dispersion of the data points, low value indicates high stability (low variability) and vice versa.

Defining robustness is not straightforward, but as stated in the systematic review about stability assessment of radiomic features by Traverso et al. [10] *repeatability* and *reproducibility* are two key elements. Repeatability refers to the degree of which features remain unchanged under the same imaging conditions, e.g. the same subject is being scanned multiple times with the same scanning parameters, equipment etc. Reproducibility means that features stay unchanged under various imaging conditions, i.e. using different equipment, image acquisition parameters, same imaging parameters but different subjects and so on [10] [20]. Features fulfilling both of these requirements, i.e. having a high stability (low variability) under unchanged conditions as well as for different subjects, ROI and/or imaging parameters, will be classified as robust or stable.

3.2.5 (v) Building predictive models

With the hypothesis that quantitative image analysis can detect underlying patterns in medical images revealing pathophysiology, the final aim of radiomics is to create predictive models for improving decision support [7]. Model building can be done using statistical methods, machine learning or artificial intelligence [6] but in common for all is the need of large and integrated databases [11]. One of the main challenges for creating these predictive models is the limited possibility of sharing image and patient data across institutions [6]. There are different approaches on how to deidentify confidential information according to patient safety regulations, but no common ground has yet been found [11] [6].

3.3 Radiomic features

As mentioned previously, a limitation in the field of radiomics is that there is no existing standardization and the lack of reproducibility. IBSI is an independent international collaboration working to provide standard biomarker nomenclature, definitions, image processing workflow etc for the radiomic process [24]. Quantitative imaging biomarkers, or features, are described in the IBSI manual as indicators of pathophysiological processes and the aim is to find common guidelines in how to interpret and use them.

An important aspect of radiomics is that imaging features can be derived from the entire tumor (or other volume of interest) and not a single sample. However, heterogeneous sections of the tumor, so-called *habitats*, can be chosen as well. Once a volume of interest has been segmented a large number of features can be extracted, which are divided into "semantic" and "agnostic" descriptors of the volume [6]. *Semantic* features are used in today's clinics as a tool for radiologists to qualitatively describe lesions such as size and shape descriptors. However, some of these features can be extracted quantitatively as well [6] [12]. *Agnostic* features are solely quantitative descriptors of the region of interest, characterizing the voxel intensity histogram, texture patterns and so on [11]. Furthermore, quantitative features can be categorized into first, second and higher order features [18]. Each feature category will in the following subsections be described into further detail.

3.3.1 Shape-based features

Shape-based features describe the geometric properties of the ROI and are based on ROI voxel representations of the volume [24]. There are three voxel representations defined in the IBSI standardization manual accordingly:
1. The volume is represented by a collection of voxels with each voxel taking up a certain volume.
2. The volume is represented by a voxel point set $\mathbf{X}_c$ that consists of coordinates of the voxel centers.
3. The volume is represented by a surface mesh.

The first definition does not handle partial volume effects at the ROI edge well and is therefore not recommended to be used for purposes other than volume approximations. When the inner structure of the ROI is of importance the second representation should be used. A mesh-based representation connects points in space (vertices) generating triangle meshes to cover the ROI, allowing for a more consistent surface representation than a voxel-based representation. Thus, the third definition should be used when the outer surface is important [24].

Tumor compactness, surface area, volume etc are examples of features that can be extracted. Surface-to-volume ratio is an example of an important characteristic that is used to differentiate between a speculated tumor (higher value) from a more round tumor (lower value) with the same volume [11]. Feature values are calculated according to the unit of length defined in the DICOM standard [24]. Features within the category "Long & Short axis" should also be included in the shape-based definition, but are in this work calculated in a separate group.

3.3.2 First order statistics

First order statistical features describe the distribution of voxel intensities within the ROI without taking the spatial distribution between them into account [6]. There are solely intensity based features that do not require discretisation. However, these features lack meaning if an arbitrary intensity scale is being used [24]. Intensity histogram based features are similar descriptors, but the selected 3D volume data is in this case first reduced into a histogram by discretisation of the intensity distribution into intensity bins. Examples of descriptors that can be calculated from intensity/intensity histogram distributions are mean intensity, min, max, kurtosis, interquartile range and other common statistics [24] [11].

3.3.3 Second order statistics

While first order statistics do not provide any information about patterns in the image, the second order features do. They are also known as texture features and describe how combinations of voxels with similar intensities are distributed along different directions [6] [24]. The assumption is that texture information not visible for the naked eye can be found in the spatial distribution between voxel intensities [25]. The second order features are therefore derived from so-called *gray-tone spatial-dependence matrices* that describe distances and different directional relationships between neighboring voxels [26].

Gray level co-occurrence based features

A gray level co-occurrence matrix (GLCM) describes the distribution of intensities in neighboring resolution cells. This analysis is applicable on both 2D images and 3D volumes but following examples will be considered in 2D for simplicity [24]. The formation of a GLCM is based on so-called nearest-neighbor resolution cells where a pixel has eight neighboring pixels (except at the periphery) [26], shown in figure 2. The probability of finding a pixel with gray level value i at distance d and angle θ from a pixel with gray level value j is denoted $P(i,j,d,\theta)$ [25].

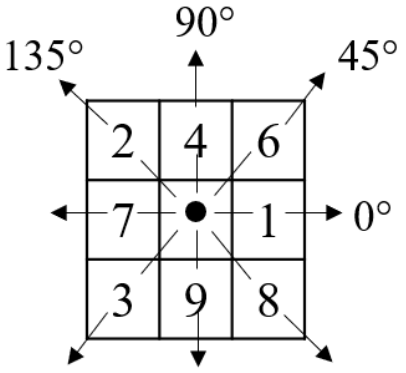

Figure 2: Two-dimensional nearest-neighbor resolution cell. Each pixel, except at the margin, has eight neighboring pixels.

Consider the following example; a rectangular image with 4x4 pixels and 4 discrete gray levels 0 to 3 as shown in figure 3. If d=1, let $\mathbf{M}_\theta(i,j)$ be the 4x4 GLCM where θ is the directional vector and i, j a combination of intensities in neighboring resolution cells. This means that e.g. the element $M_{0^\circ}(1,2)$ in the GLCM will denote how many times gray level 1 and 2 occur alongside each other in the horizontal direction in the image. Thus, $M_{0^\circ}(i,j)$ is the final resulting matrix in the horizontal direction, $M_{45^\circ}(i,j)$ in the 45° direction and so on. The final matrices calculated from this simple example can be seen in figure 4.

2	0	1	3
1	2	2	1
3	1	1	0
2	2	1	1

Figure 3: A 4x4 image with 4 discrete gray levels, ranging from 0 to 3.

After computation of a matrix in each direction, the subsequent step is to normalize the GLCM so that each element will represent the probability of acquiring a certain combination of neighboring gray levels [27]. The normalized matrix $\mathbf{P}_\theta(i,j)$ is derived by dividing each entry by the total sum of entries in each matrix (see example in figure 5 (a) and (b)) [24] [26].

		j			
	0°	0	1	2	3
	0	0	2	1	0
i	1	2	4	3	2
	2	1	3	4	0
	3	0	2	0	0

		j			
	90°	0	1	2	3
	0	0	2	1	0
i	1	2	2	5	2
	2	1	5	0	1
	3	0	2	1	0

		j			
	45°	0	1	2	3
	0	0	2	0	0
i	1	2	2	4	0
	2	0	4	0	2
	3	0	0	2	0

		j			
	135°	0	1	2	3
	0	0	0	2	0
i	1	0	8	1	0
	2	2	1	2	1
	3	0	0	1	0

Figure 4: The four final directional gray co-occurrence matrices calculated from the example 4x4 image.

With the initial assumption that texture information is found in the GLCM [26], feature values are derived from the normalized GLCM as a final step. The GLCM features are descriptors relating to contrast, homogeneity and other textural characteristics of the image [26]. IBSI describe six different methods to aggregate the features, e.g. features can be computed from each 2D directional matrix and then averaged over 2D direction and slices or features can be computed from a single matrix after merging all 3D directional matrices. However, feature values may vary depending on method [24].

		j				
	0°	0	1	2	3	$\sum_j$
	0	0	2	1	0	**3**
i	1	2	4	3	2	**11**
	2	1	3	4	0	**8**
	3	0	2	0	0	**2**
		3	**11**	**8**	**2**	**24**

(a)

		j				
	0°	0	1	2	3	p_i
	0	0	0.08	0.04	0	**0.13**
i	1	0.08	0.17	0.13	0.08	**0.46**
	2	0.04	0.13	0.17	0	**0.33**
	3	0	0.08	0	0	**0.13**
p_j		**0.13**	**0.46**	**0.33**	**0.08**	**1.00**

(b)

Figure 5: The GLCM for the 0° direction (a); and the corresponding normalized matrix $\mathbf{P}_\theta(i,j)\mathbf{P}_{0^\circ}(i,j)$ in the same direction (b).

Gray level run length based features

The gray level run length matrix (GLRLM) is another method, similar to the GLCM, to describe various patterns and texture features in an image. The matrix $\mathbf{R}_\theta(i,j)$ is computed in a similar approach, based on the resolution cell intensity distribution within the image [24]. However, rather than identifying combinations neighboring gray level pairs a run-length is defined as the number of consecutive pixels having the same gray level value along a certain direction [28]. The probability of finding run length j with intensity i in direction θ is then denoted $P(i,j,\theta)$. Using the same 4x4 pixel image, shown in figure 3 as an example, will result in the subsequent matrices seen in figure 6. Normalization and feature extraction is then done analogous to the procedure mentioned in the GLCM section. Quantitative descriptors such as short and long run emphasis or gray level non-uniformity can be extracted from the GLRLM [11]. Feature values are again dependent on the aggregation method [24].

		j			
	0°	1	2	3	4
	0	2	0	0	0
i	1	3	2	0	0
	2	1	2	0	0
	3	2	0	0	0

		j			
	90°	1	2	3	4
	0	2	0	0	0
i	1	5	1	0	0
	2	5	0	0	0
	3	2	0	0	0

		j			
	45°	1	2	3	4
	0	2	0	0	0
i	1	5	1	0	0
	2	5	0	0	0
	3	2	0	0	0

		j			
	135°	1	2	3	4
	0	2	0	0	0
i	1	0	2	1	0
	2	3	1	0	0
	3	2	0	0	0

Figure 6: From the example 4x4 are the following four directional gray level run length matrices computed.

Gray level size zone based features

IBSI describes the gray level size zone matrix (GLSZM) as the count of neighboring pixels (or voxels in 3D) within an image. A group, or zone, is defined as the number of linked pixels having the same gray level [24]. An element in the GLSZM **Z(i,j)** is then defined as the number of times a zone of size j with intensity i occurs within an image. As opposed to the GLCM and GLRLM, where the directional vector leads to four matrices, only one matrix is generated from the whole image. Using the image in figure 3 as an example again results in the matrix shown in figure 7. IBSI then defines three methods to aggregate features from the resulting matrix, where feature definitions are similar to the GLRLM descriptors [24].

		j						
		1	2	3	4	5	6	7
i	0	2	0	0	0	0	0	0
	1	0	0	0	0	0	0	1
	2	0	1	1	0	0	0	0
	3	2	0	0	0	0	0	0

Figure 7: The resulting gray level size zone matrix based on the example 4x4 image.

Neighborhood gray tone difference based features

The neighborhood gray tone difference matrix (NGTDM) **G(i,$\bar{A}_i$,d)** describes the difference between a pixel with gray level value i and the average intensity $\bar{A}_i$ of its neighboring pixels within distance d. The sum of intensity differences is represented by the elements in the NGTDM. A distance $d = 1$ will result in 8 neighboring pixels and is therefore defined as a valid neighborhood. If a pixel k with gray value i has a valid neighborhood the elements s_i are computed accordingly (equation 2):

$$s_i = \sum_{k}^{N} |i - \bar{A}_i| \tag{2}$$

2	0	1	3
1	2	2	1
3	1	1	0
2	2	1	1

Figure 8: Each pixel within the rectangle boundary is defined as having a valid neighborhood. The NGTDM is computed based on these pixels and their neighboring pixels.

where N here is defined as the number of pixels within the ROI and the valid neighborhood. Using the same 4x4 image in figure 3 as an example, pixels having a valid neighborhood are located within the rectangle (see figure 8). The resulting NGTDM is shown in figure 9 where n_i is number of pixels with intensity i, $p_i = n_i/N$

is the gray level value probability and s_i the neighborhood gray level difference. From this matrix features such as coarseness, contrast, complexity and so on can be extracted. The above description was based solely on the IBSI definitions [24].

		n_i	p_i	s_i
	0	0	0	0
i	1	2	0.5	1
	2	2	0.5	1.5
	3	0	0	0

Figure 9: The final neighborhood gray tone difference matrix based on the 4x4 image with a defined neighborhood.

Laws' texture energy measure

This is another approach to analyze underlying texture patterns in an image by using convolution kernels, also referred to as convolution masks. The method is meant to capture the amount of variation within the image, i.e. the texture energy [29]. The convolution masks are generated by combinations of the following three vectors [30]:

$$\begin{aligned} L3(Level) &= [\ 1, \quad 2, \quad 1\ ] \\ E3(Edge) &= [-1, \quad 0, \quad 1\ ] \\ S3(Spot) &= [-1, \quad 2, \quad -1] \end{aligned} \tag{3}$$

The purpose of each vector is written within brackets; L3 gives a center-weighted local average, E3 detects edges in the image and S3 detects spots [29]. A mask is a kernel, or filter, emphasizing different structures in the image depending on the specific combination of L3, E3 and S3 in the x-, y- and z-direction. They are generated by convolution of the vectors leading to nine two-dimensional masks with length three and 27 three-dimensional masks generated by 2D and 3D convolution, respectively. The masks are then applied to the image to extract quantitative descriptors [30].

3.3.4 Higher order statistical features

These methods utilize filters or mathematical transforms on the image to i.a. identify repetitive/non-repetitive patterns, reduce noise or extract details [6] [12]. There are different methods to perform higher order statistical analysis including e.g.

wavelet transforms, fractal analysis and Laplacian transforms of Gaussian-filtered images [12], which will be described into further detail below.

Wavelets

The idea behind the wavelet analysis is to obtain a time-frequency representation of the signal. A wavelet has oscillating properties but is better described as a "small wave" with a finite energy concentrated in time [31]. Wavelets have similar properties as band-pass filters [32], meaning that they allow frequencies within a certain span to pass and attenuate frequencies outside of that range. Different combinations of low- (L) and high-pass (H) filters can be obtained in three-dimensional wavelet transform, emphasizing various patterns and structures in the image. As an example, HHL indicates a wavelet transform using high-pass filters in the x- and y-direction and a low-pass filter in the z-direction [33]. The image is multiplied with a matrix of these complex small waves to extract certain patterns [6].

Fractal analysis

Fractals are structures in the image having repeating patterns at different size scales [34]. In fractal analysis patterns are imposed on the image and the number of elements with a certain gray level value can then be identified [6]. The parameter of quantification is called fractal dimension and this type of analysis has shown to be a reliable method for tumor heterogeneity characterization [34].

Laplacian transforms of Gaussian-filtered (LoG) images

This is a more straightforward analysis method used to extract areas with coarse texture, were a Gaussian bandpass filter is applied to the image followed by a Laplacian filter [6].

4 MATERIALS AND METHODS

4.1 Phantom properties

4.1.1 Magphan® RT phantom

One part of the phantom feature analysis was performed on images from the monthly QA of the integrated MRI-Linac, acquired with the Magphan® RT phantom (see figure 10 (a) and (b)). The phantom has two modules, bottom (TMR007) and top (TMR009), containing a uniform background fill solution and several hundred 1 cm sphere fiducials and other solid test components. The background fill solution consists of 96.4 % distilled water, 2.5 % PVP, 0.9 % Sodium Chloride, < 0.2 % Potassium Sorbate, < 0.2 % Copper Sulfate and < 0.2 % Blue Food color defined in percentage by weight. This results in T1 and T2 values about 175-225 ms at 0.35 T [35] [36].

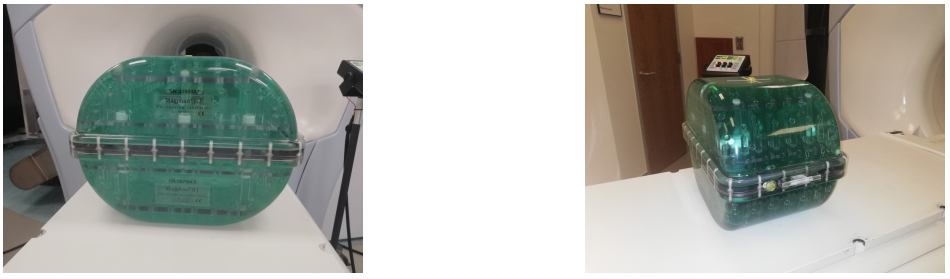

(a) (b)

Figure 10: The Magphan® RT phantom used for the monthly image acquisition dataset.

4.1.2 ViewRay Daily QA phantom

The ViewRay Daily QA phantom is a cylindrical phantom filled with distilled water to ensure MR imaging properties. The phantom has outlined markings for laser alignment that coincides with the active volume of an ionization chamber, which can be placed in a central chamber position. Four additional chamber positions exist at the periphery [37]. The phantom is shown in figure 11 (a) and (b).

4.2 Data selection and image acquisition

The purpose of the phantom studies was to investigate the variability of radiomic features over time in an invariant object. Hence, the aim of the data collection was to represent ideal imaging conditions and thereby identify features that are robust

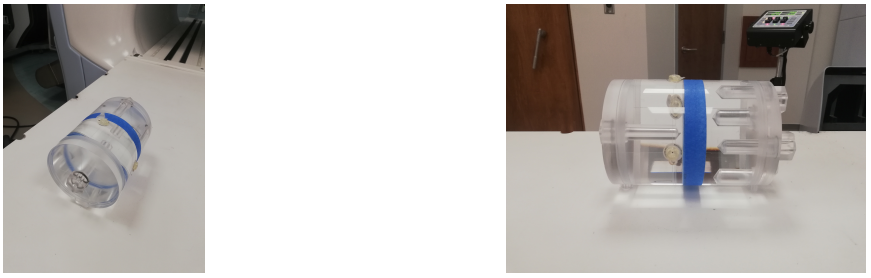

(a) (b)

Figure 11: The ViewRay Daily QA phantom used for the daily image acquisition dataset.

under these conditions. Eleven scans acquired over a 13-month period using a Magphan® RT phantom, and 11 workdays using a ViewRay Daily phantom respectively, constituted the phantom data. The phantom positioning and set-up were identical for every scanning occasion for both phantoms using a Torso coil and a high resolution TRUFI pulse sequence. Following imaging parameters were used; (1.5mm x 1.5mm x 1.5mm) resolution, (500mm x 449mm x 432mm) FOV and 172 s total image acquisition time.

The patient dataset included 50 images from ten anonymized stereotactic body radiation therapy (SBRT) pancreas cancer patients treated on the integrated MRI-Linac (5 fractions, given on a daily basis). All images were acquired with a Torso coil and TRUFI pulse sequence with a (1.5mm x 1.5mm x 3.0mm) resolution, (540mm x 465mm x 432mm) FOV and a 25 s total imaging time.

4.3 Image registration and segmentation

Image import, export, segmentation and registration was done in Mirada RTx (Mirada RTx 1.6, Mirada Medical, Oxford, UK). For the phantom data the first scan in chronological order was used as the baseline imaging set in which the contours were drawn with a manual segmentation tool. Identical cylindrical ROIs with a volume of 4.2 cm^3 were contoured in different sections of the two phantoms. Four regions displaying interesting heterogeneous patterns were chosen in the Magphan® RT phantom and two heterogeneous regions in the ViewRay Daily phantom. Contours are shown in figure 12 (a)-(d). All structures were then propagated from the baseline to the remaining ten imaging sets by rigid registration in Mirada RTx.

As a transition between ideal imaging conditions in the phantom data to a more complex structure such as human tissue, the kidneys and liver were chosen to represent heterogeneous but theoretically invariant objects in the patient, i.e. with the

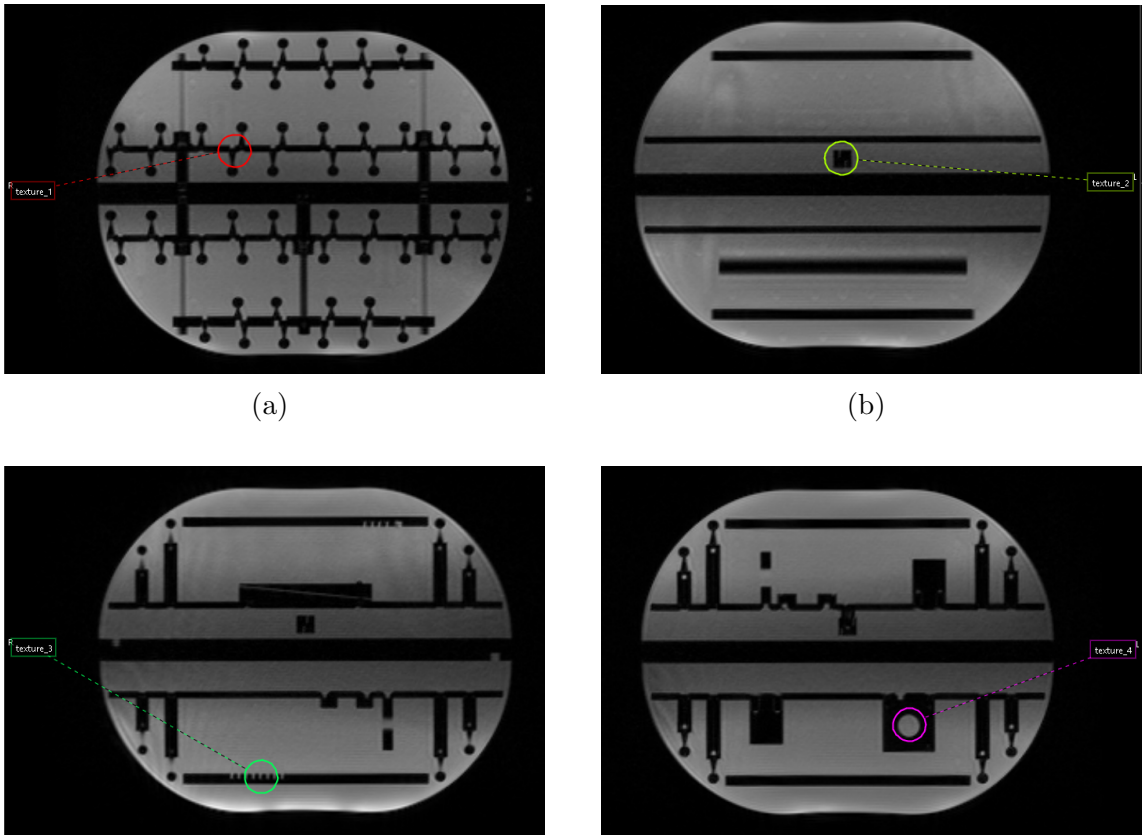

(a) (b)

(c) (d)

Figure 12: Four identical ROIs were placed in the Magphan® RT phantom, in regions displaying interesting heterogeneous patterns.

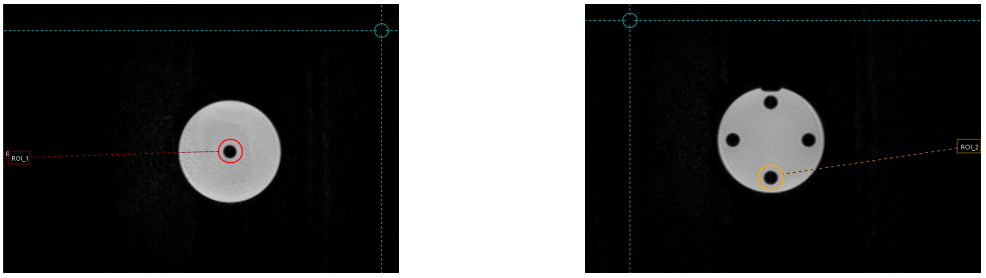

(a) (b)

Figure 13: Two identical ROIs were placed in the ViewRay Daily QA phantom, in regions displaying heterogeneity.

hypothesis that these organs not were affected by the radiation during the treatment. Both kidneys were manually segmented in Mirada RTx for each scanning occasion and patient, shown in figure 14. A spherical 14 cm^3 ROI was placed 4 cm caudally from the diaphragm, 11 cm laterally from the aorta and in the midsection in the anterior/posterior direction so that the relative placement within the liver for each patient was identical (see figures 15 a) and b)).

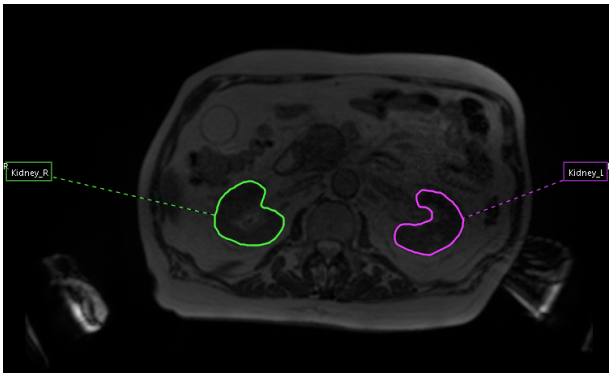

Figure 14: The kidneys were manually segmented for each scanning occasion and patient.

Hence, four final datasets were defined for further analysis: monthly phantom, daily phantom, patient kidney data and patient liver data. The experimental setup was similar to a "classical" test-retest setup. However, instead of comparison between two nearly identical images solely, this setup included comparison between several intrasubject as well as intersubject images in order to identify robust features. The aim was to identify common robust radiomic features among all datasets.

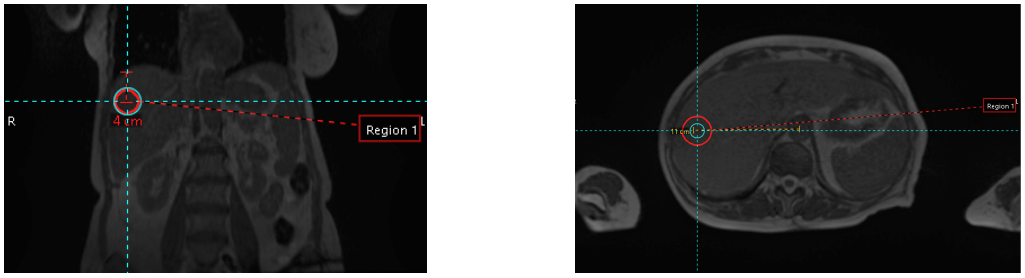

(a) (b)

Figure 15: A spherical 14 cm^3 ROI was placed in a defined position in the liver for each scanning occasion and patient.

4.4 Statistical analysis workflow

Feature extraction was performed using an in-house program, based on the definitions from IBSI and those found in the work by Shafiq-ul-Hassan et al. [14], that aggregated 1087 radiomic features (48 categories). A summary of all groups can be seen in table 1 with total number of features written within brackets. The DICOM-file and structure set(s) for each scanning occasion and subject had to be uploaded manually in the program one by one. The extracted feature values were then summarized in an excel spreadsheet and organized for each phantom/patient dataset accordingly for further analysis. An outline of the statistical analysis workflow after feature extraction is shown in figure 16.

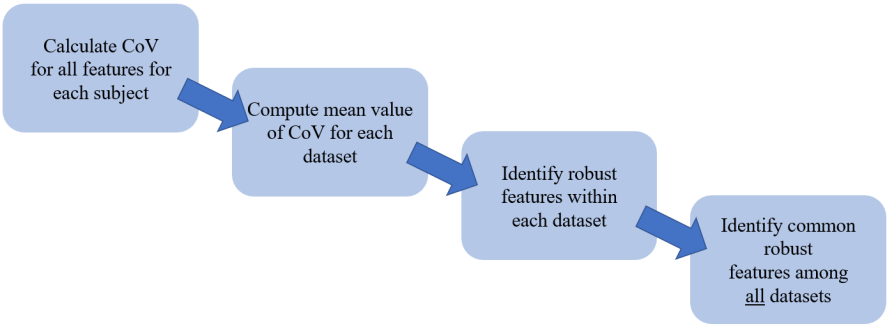

Figure 16: Statistical analysis workflow.

Stability was assessed with the Coefficient of Variation defined in equation 1. A boundary for feature stability was set to CoV<5%, i.e. features that fall under this limit were classified as robust. The limit was based on similar work done by Molina et al. [23] and Rai et al. [20] using CoV<10% and CoV<5%, respectively, to assess feature stability. The stricter confinement was chosen accordingly.

Statistical analysis included five daily setup images from 10 different patients as well as 11 images each from two different phantom, and multiple ROIs in all subjects. The CoV was therefore a suitable statistical descriptive measure in this experimental setup, allowing for a straightforward methodology to identify robust features among all the datasets, fulfilling both of the stability requirements. First, the CoV measures the degree of variability for all features within each subject individually, i.e. identifying features fulfilling the repeatability requirement. Second, by calculating the mean value of the CoV for each feature in every dataset and identifying common features that are stable over various imaging conditions, the CoV will capture the degree of reproducibility as well.

Once radiomic features were extracted for every scanning occasion and ROI for each subject, the CoV for all 1087 radiomic features was calculated for the two phantoms and all patients individually. Then, the mean value of the CoV for every feature in each dataset (kidney, liver, monthly phantom and daily phantom separately) was computed. Features with no value, i.e. 0 for each scanning occasion were excluded from further analysis. Lastly, features with a CoV mean value categorized as robust (CoV$< 5\%$) were identified for each dataset, and common robust features among all four datasets were identified as a final step.

Table 1: List of all feature categories that were analyzed, with number of features within each group written within brackets.

Feature category	
Intensity&Shaped based (70)	Laws SEE (22)
Long&Short axis (22)	Laws SEL (22)
Co-occurrence (40)	Laws SES (22)
Run-length (17)	Laws SLE (22)
Gray level size zone (12)	Laws SLL (22)
Neighborhood gray tone diff. (11)	Laws SLS (22)
Laws EEE (22)	Laws SSE (22)
Laws EEL (22)	Laws SSL (22)
Laws EES (22)	Laws SSS (22)
Laws ELE (22)	Wavelet HHH (22)
Laws ELL (22)	Wavelet HHL (22)
Laws ELS (22)	Wavelet HLH (22)
Laws ESE (22)	Wavelet HLL (22)
Laws ESL (22)	Wavelet LHH (22)
Laws ESS (22)	Wavelet LHL (22)
Laws LEE (22)	Wavelet LLH (22)
Laws LEL (22)	Wavelet LLL (22)
Laws LES (22)	Fractal dimension (6)
Laws LLE (22)	LoG sigma=0.5mm (22)
Laws LLL (22)	LoG sigma=1.0mm (22)
Laws LLS (22)	LoG sigma=1.5mm (22)
Laws LSE (22)	LoG sigma=2.0mm (22)
Laws LSL (22)	LoG sigma=2.5mm (22)
Laws LSS (22)	LoG sigma=3.0mm (22)

5 RESULT

After statistical analysis 130 radiomic features were identified as demonstrating high stability in both phantom and patient data. All final robust features within each category are shown in table 2. Stable features were found within every category apart from two second order statistics groups: Gray level size zone and Neighborhood gray tone difference. The variability, expressed as the mean value of the CoV, for each robust feature in every dataset is presented graphically in figures 17-21. The exact CoV mean values and the corresponding standard deviations for each feature are summarized in tables 3-10 in Appendix.

Table 2: Table demonstrating the resulting 130 radiomic features that were identified as being robust in both human and phantom data.

Long & Short axis	**Intensity & Shaped based**	**LoG sigma=0.5mm**
LongAxis(mmCOM)	V(voxels)	Energy
Maximum 3D diameter(mm)	Volume	Entropy
	Surface area	Hist entropy
LoG sigma=1mm	Surface to volume ratio	Norm energy
Entropy	Volume density(axis)	Norm entropy
Hist entropy	Area density(axis)	
Norm Entropy	Volume density(convex)	**LoG sigma=1.5mm**
	Area density (convex)	Coeff vari
LoG sigma=2mm	Sphericity	Energy
Coeff vari	Asphericity	Entropy
Energy	Compactness 1	Hist entropy
Entropy	Spherical disproportion	Norm energy
Hist entropy	Volume fr. at 0.10 intensity	Norm entropy
Norm energy	NIenergy	
Norm entropy	Entropy	**LoG sigma=2.5mm**
	Hist entropy	Coeff vari
LoG sigma=3mm	Norm NIenergy	Energy
Coeff vari	Norm entropy	Entropy
Energy		Hist entropy
Entropy	**Wavelet LLL**	Norm energy
Hist entropy	Coeff vari	Norm entropy
Norm energy	Energy	
Norm entropy	Entropy	**Wavelet LLH**
	Hist entropy	Coeff vari

Continued on next page

Table 2 – continued from previous page

Wavelet LHL	Norm energy	Entropy
Entropy	Norm entropy	Hist entropy
Hist entropy		Norm entropy
Norm entropy		
	Wavelet HLL	**Wavelet LHH**
Wavelet HLH	Entropy	Entropy
Entropy	Hist entropy	Hist entropy
Hist entropy	Norm entropy	Norm entropy
Norm entropy		
	Wavelet HHL	**Wavelet HHH**
Laws EEE	Entropy	Coeff vari
Hist entropy	Hist entropy	Energy
		Entropy
Laws EEL	**Laws EES**	Hist entropy
Hist entropy	Hist entropy	Norm energy
		Norm entropy
Laws ELE	**Laws ELL**	
Hist entropy	Hist entropy	**Laws ELS**
		Hist entropy
Laws ESE	**Laws ESL**	
Hist entropy	Hist entropy	**Laws ESS**
		Hist entropy
Laws LEE	**Laws LEL**	
Hist entropy	Hist entropy	**Laws LES**
		Hist entropy
Laws LLE	**Laws LLL**	
Hist entropy	Energy	**Laws LLS**
	Entropy	Hist entropy
Laws LSE	Hist entropy	
Hist entropy	Norm energy	**Laws LSL**
	Norm entropy	Hist entropy
Laws LSS		
Hist entropy	**Laws SEE**	**Laws SEL**
	Hist entropy	Hist entropy
Laws SES		
Hist entropy	**Laws SLE**	**Laws SLL**
	Hist entropy	Hist entropy

Continued on next page

Table 2 – continued from previous page

Laws SLS Hist entropy **Laws SSS** Hist entropy **Gray-level size-zone** - **Nbrhood. Gray-Tone Diff.** -	**Laws SSE** Hist entropy **Co-occurrence** Entropy Mean Inverse diff. moment Inverse diff. Sum entropy Vnorm Mean Gnorm Mean Gnorm Sum Entropy Gnorm Mean VGnorm Mean	**Laws SSL** Hist entropy **Run-length** SRE LRE RLNU RPC **Fractal dimension** meanLac1 meanLac2 meanLac3

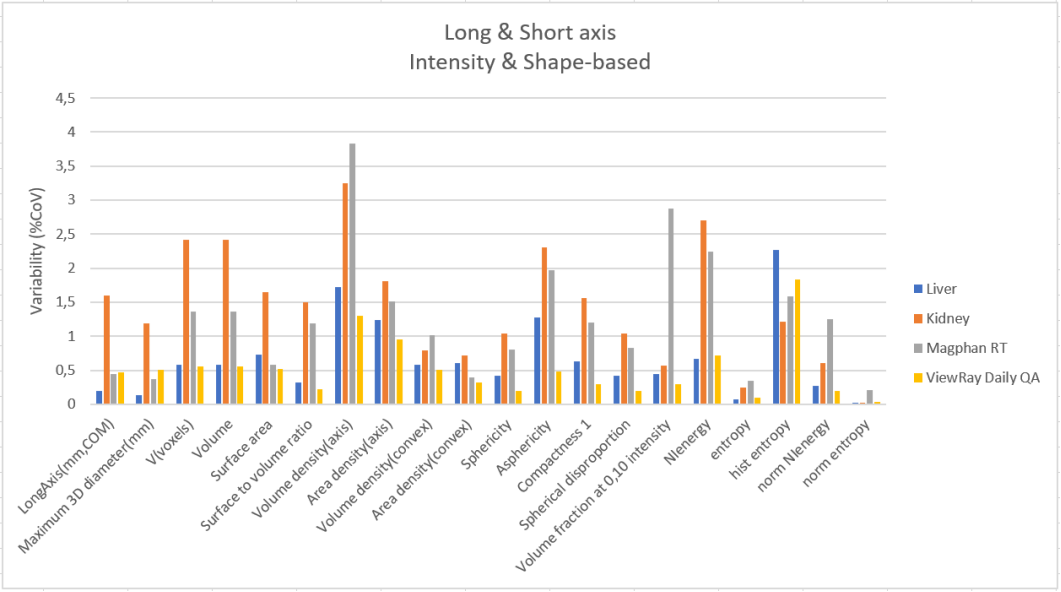

Figure 17: Graphical representation of the variability for all robust radiomic features in each dataset. Presented in this chart are features from the Long&short axis and Shaped-based categories.

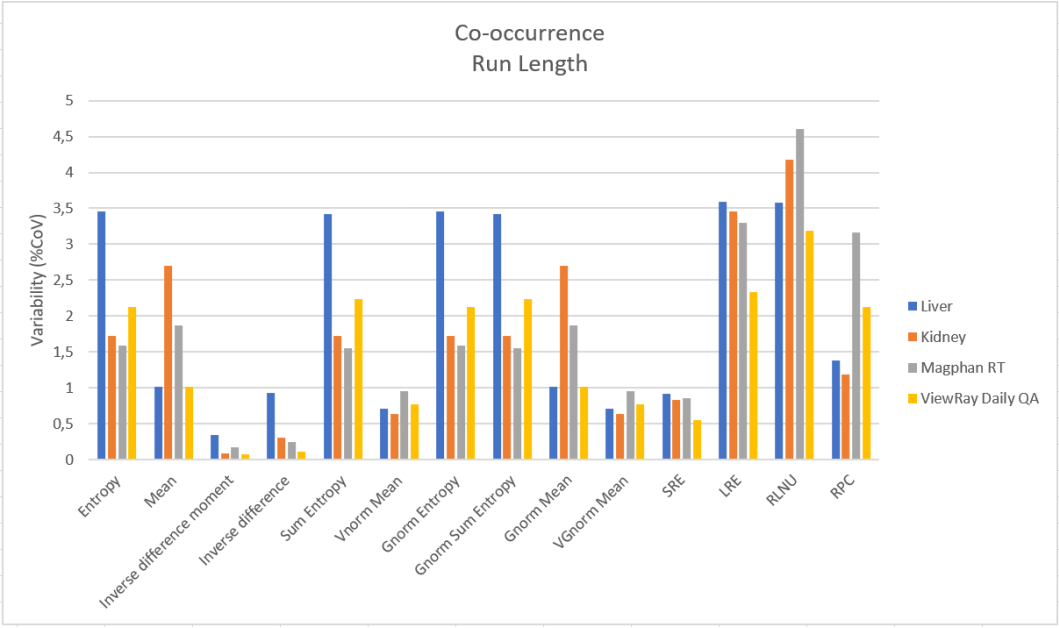

Figure 18: Graphical representation of the variability for all robust radiomic features in each dataset. Presented in this chart are features from the Co-occurrence and Run Length categories.

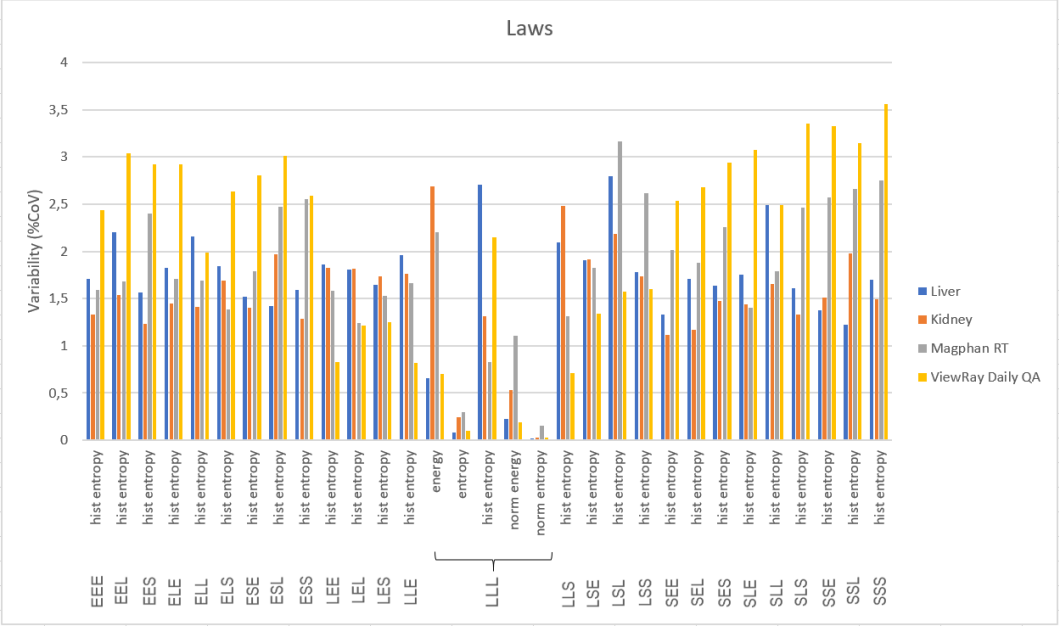

Figure 19: Graphical representation of the variability for all robust radiomic features in each dataset. Presented in this chart are features from the Laws category.

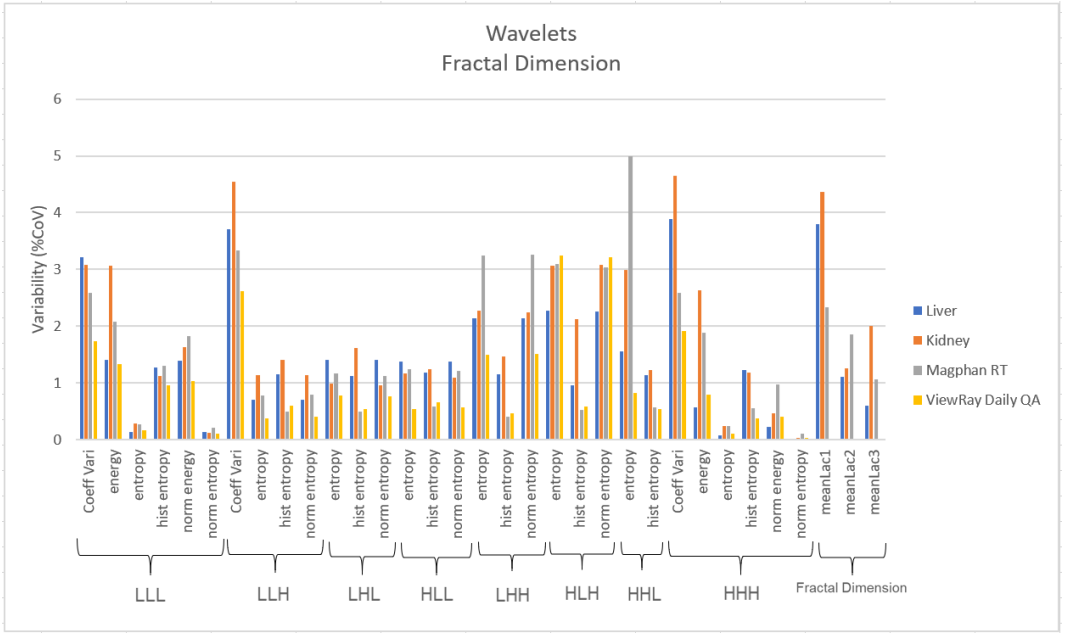

Figure 20: Graphical representation of the variability for all robust radiomic features in each dataset. Presented in this chart are features from the Wavelet and Fractal dimension categories.

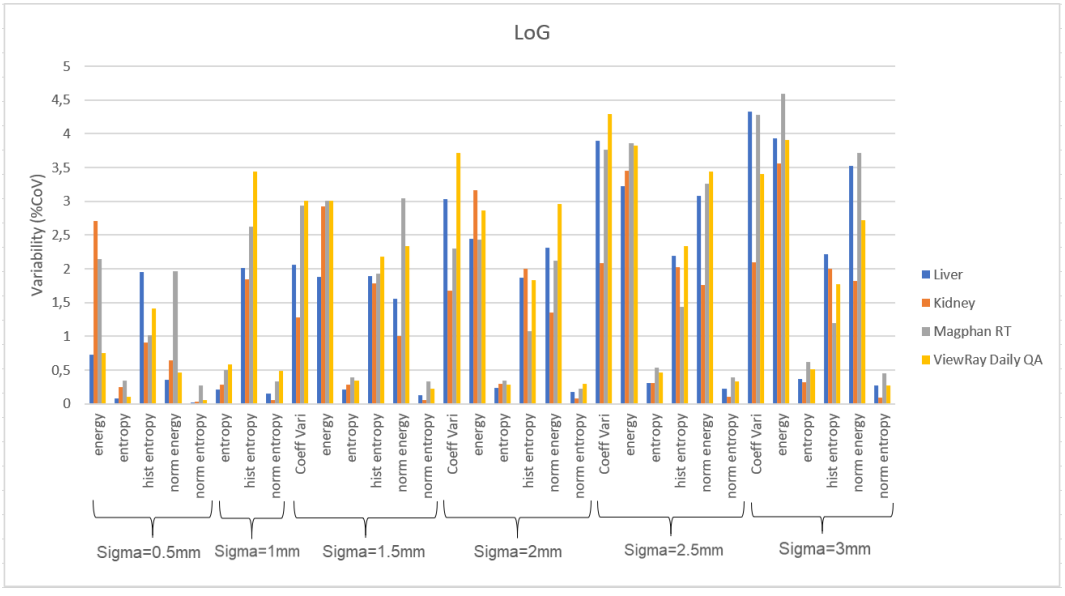

Figure 21: Graphical representation of the variability for all robust radiomic features in each dataset. Presented in this chart are features from the LoG category.

6 DISCUSSION

6.1 Stability of MRI-based Radiomics

Currently, little work has been done on stability assessment for MRI-based radiomics and more research is required [18]. The purpose of this section is to give a brief summary of a few available studies and compare the results with the outcome of this thesis. Studies with similar questions, aim, method or other findings relevant to this work were selected to add valuable information.

In an article by Cattell et al. [18] they describe a phantom study mapping the variability of radiomic features on images acquired on a 3 T system under various conditions. The phantom was composed of a pineapple core, banana, orange, strawberry and kiwi placed on a Styrofoam box. They looked at first order, shape, GLCM and GLRLM features and used the intraclass correlation coefficient (ICC) as measure of variability. The study included evaluation of feature robustness to signal-to-noise ratio (SNR), ROI delineation, small voxel size variation and different normalization methods. Most first order features were found to be robust against variations of SNR, erosion of the ROI, while moderately to highly robust against dilation of the ROI and pixel size variations. All shape-based features showed robustness against pixel size variation as well as the two ROI delineation methods. Most GLCM and GLRLM features were moderately robust against SNR variations but had higher stability against variations in delineation. Eight robust features in common with the result of this thesis and their study were identified: Sphericity and Spherical disproportion (shape-based), Inverse difference and Sum entropy (GLCM) and SRE, RPC, LRE and RLNU (GLRLM).

Padgett et al. [22] did a variability study on radiomic features extracted from images from a ViewRay 0.35 T MRI system, similar to the one in this thesis. They used an ACR-MR phantom and selected six different regions of interest demonstrating various interesting patterns for extracting radiomic features. The high resolution protocol with 1.5mm^3 voxel resolution was used to acquire 12 scans collected over a 6-months period. They investigated the robustness of 8 geometric features and 34 first and second (GLCM) order features with the Coefficient of Variation as the measure of stability. A fixed bin width was used to extract the first order features, while the stability of the GLCM features were analyzed using different number of bins as well as varying bin size. All of the geometric features were found to be stable, of which four are in agreement with the result in this work; Surface area, Surface to volume ratio, Compactness 1 and Spherical disproportion. Furthermore, they found that using different number of fixed bins had less impact (i.e. lead to a more robust result) on second order feature variability than when varying bin width. However, most first and second order features had a variation between 20% to 30% and only

two features apart from the geometric ones had a comparable level of robustness as the stable features that were found in this thesis: Hist entropy (first order) and Entropy (GLCM).

Molina et al. [23] explored the stability of textural features in pretreatment 3D T1-weighted MR images (3 T system) by studying patients harboring glioblastoma. The stability of sixteen GLCM and GLRLM features were investigated when changing the dynamic range (number of gray level values) and matrix size (spatial resolution). Robustness was assessed with the Coefficient of Variation with CoV<10% as the limit for stability, compared to CoV<5% in this thesis. They found that none of the textural features were robust when varying the number of gray level values. Only one GLCM feature, Entropy, was found to be robust when changing the spatial resolution. Hence, they conclude that due to a lack of feature stability standardization is a requirement before using these features in multi-center clinical studies. No other common robust feature, apart from GLCM Entropy, was identified between their study and this thesis.

In a recent multi-center study by Rai et al. [20] a novel radiomics phantom was designed for stability and reproducibility assessment of different MRI-scanners. They developed 3D-printed phantoms using MRI visible materials, that display various complex textures aiming to imitate the heterogeneity in human tissue. Radiomic features were extracted from the first order, shape and texture based categories. Intrascanner reproducibility was assessed with the Coefficient of Variation (CoV<5% was classified as a very small range of variation, i.e. equivalent to the level of robustness in this work) and the Intraclass Correlation Coefficient was used for stability assessment across eight different scanners. Nine features, classified in this thesis as robust, had a CoV<5%: Surface to volume ratio and Spherical disproportion (Shape), Entropy, Inverse difference moment and Sum entropy (GLCM) and SRE, LRE, RLNU and RPC (Run length). The authors stated that most stable features, when looking at interscanner stability, were found in the first-order statistics while the shape-based category had the least number of stable features. Stable texture features could be identified, but the category displayed a varied result overall. Lastly, the authors conclude that the novel 3D-printed phantom was successfully designed and can be utilized for further MRI-based radiomics analysis.

A phantom study by Buch et al. [38] compared changes in 41 radiomic features (histogram, GLCM, GLRLM, gray level gradient matrix (GLGM) and Laws) when varying magnet strength, flip-angle, number of excitations (NEX) (which has an impact on signal-to-noise ratio) and scanner platform. Changes were assessed by calculating two-tailed t-tests and corresponding P- and Q-values for each parameter and feature. They found that statistically significant changes in the Laws and most of the GLGM features were observed when varying magnetic field strength (1.5 T

vs 3 T). On the contrary, GLCM, GLRLM and histogram features were invariant to these changes. Variations in flip angle affected mostly the GLCM features, and many GLRLM, GLGM and histogram features were significantly affected by changes in NEX. However, the parameter that generated most significantly changes among all categories, except for the Laws features, was the difference in scanner platform (GE vs Siemens). They conclude that understanding how radiomic features are affected by variation of imaging parameters is important for quantitative evaluation, and highlight the need of standardized protocols. No features were stable across all the different types of variations.

In summary, these findings are promising, indicating that robust features in common to the result of this work can be found in other MRI-based radiomics studies. However, it is also an indication that feature stability assessment has been investigated to a certain extent but lacks standard methodology. The result from above mentioned studies suggest that feature values are sensitive to external factors such as spatial resolution, signal-to-noise ratio and segmentation method etc., thus emphasizing the importance to identify features that are robust across many different imaging conditions. Features must be stable enough to differentiate between pathological effects without being significantly affected by the MRI scanning parameters. The quantitative image analysis in this thesis was based on images from the MRIdian Linac which, at this moment, has a very limited set of scanning protocols. Hence, this work could provide guidelines for future stability assessment research, correlation studies or other radiomic analysis being performed on this system.

6.2 Predictive performance

The main objective of this master's thesis has been to characterize radiomic features that are robust over various imaging conditions, by comparison of both phantom and patient data. However, feature robustness does not imply that the imaging biomarker is correlated to outcome or has a predictive value [18]. The following sections therefore discuss possible predictive performance of the features found to be robust (table 2) based on MRI radiomics literature studies.

Boldrini et al. [39] evaluated the use of "delta radiomics" (the study of radiomics features variation over time) on rectal cancer patients being treated with an 0.35 T integrated MRI-Linac system, similar to the one in this thesis. They looked at 53 different shaped, statistical, fractal and textural (GLRLM) based features and correlated them with clinical complete response (cCR) to state their predictive performance. Delta features were defined as the ratio of feature values between each treatment fraction (5 fractions + 1 simulation) and the simulation. Predictive ability was assessed with the Wilcoxon-Mann-Whitney test. Six simulation features and 57

delta features were found to be significant in their discrimination between cCR and not-cCR patients. Nine common features, identified as robust in this thesis, also had a predictive value: Volume, Sphericity, Asphericity, Compactness 1, Spherical disproportion (shape), and SRE, LRE, RLNU and RPC (GLRLM).

In a study by Spraker et al. [40] they investigated whether MRI radiomic features are independently associated with overall survival (OS) in soft tissue sarcoma. Thirty radiomic features from 5 categories; tumor volume, intensity histograms, GLCM, NGTDM and GLSZM, were extracted from T1-weighted contrast enhanced MR images. A univariate analysis was performed, using Cox proportional hazard model to explore the correlation between OS and imaging feature. Four significant features common to this work were identified: Volume (Shape), Hist entropy (Intensity histogram) and Entropy and Inverse difference moment (GLCM). However, the authors were interested in multivariate analysis and looked at the association between OS and a clinical-only model, radiomics-only model and combined model, respectively. Number of radiomic features were reduced before model training by assessing collinearity using R^2 statistic. Apart from Volume (Shape) no common features between their result and this thesis were found after feature selection.

The textural feature GLCM Entropy, which was classified as robust in this work, was a notable feature as it has been shown to have high predictive performance in several studies [41] [42] [43] [44] [45] [46]. Three studies [41] [42] [43] performed texture analysis on contrast-enhanced breast MRI images and identified GLCM entropy to be one of the most significant features for discrimination between benign and malignant lesions. Wibmer et al. [44] looked at texture analysis of prostate MRI for cancer detection and Gleason score assessment. Again, GLCM entropy was found to be a significant classifier for differentiation between non-cancerous and malignant prostate tissue with different Gleason scores. Two additional studies investigated prostate cancer detection as well, one with computed-assisted diagnosis [45] and the other in pre-operative MRI images [46], and stated Entropy on T2-weighted images as one of the features with most discriminant power. *In summary, this indicates that GLCM Entropy is a feature with discriminative power in several studies, and has a high stability in images from a 0.35 T integrated MRI-Linac.*

Furthermore, the textural feature Inverse difference moment (GLCM) was identified in two of the above mentioned studies [46] [42] as having high predictive value, as well as Sum entropy (GLCM) in the study by Viswanath et al. [46]. Both of these features were found to be stable in this work.

In a study by Lacroix et al. [47] they looked at radiomic features from T2-weighted MR images (3 T system) of lung cancer patients. Their aim was to find a preprocessing procedure that improves the predictive performance of the features. Images

were corrected for magnetic field inhomogeneities followed by intensity normalization with fat as a reference tissue. They looked at shape, first order and second order features extracted from the whole tumor volume (3D analysis) and from slices of the tumor (2D analysis). They concluded that number of informative features increased after image processing such as magnetic field inhomogeneity correction and voxel value normalization.

In conclusion, several radiomic features identified as robust in this work are found to have diagnostic or predictive value in different radiomic based MRI studies. Nine common features had significant predictive performance in a study done on a low-field scanner system similar to the one in this thesis, which is a promising result. GLCM Entropy, classified as robust in this work, is a feature with diagnostic significance correlated to lesion discrimination mentioned in several papers. However, as concluded by Lacroix et al. [47] the predictive value of a feature are in various cases dependent on image processing method, such as magnetic field inhomogeneity or voxel value normalization. Standardization and assessing feature robustness is therefore of great importance in order to obtain radiomic features with optimized predictive performance.

6.3 Limitations

This work has several limitations that ought to be mentioned. First, it should be noted that a phantom measurement is not fully representative of a patient study. Phantoms are often designed to mimic different parts of the body but similarities are limited to some degree, due to the complex nature of the human anatomy and the simplified phantom. The phantoms used in this work are designed for QA and do fulfill the requirements for this purpose. However, in radiomics we are interested in heterogeneous structures that simulates the complex structure of human tissue or a tumor, and the simplicity of these phantoms do not provide texture in this sense. The Magphan® RT and ViewRay Daily phantom both consist of homogeneous non-MRI visible fabrics filled with a signal generating liquid, giving rise to a more or less binary signal which is not ideal for radiomics. Results from radiomic studies might not therefore be completely translated to the texture and wide range of gray level values seen in human tissue. Nonetheless, these results represent ideal imaging conditions and can, together with patient data, give an indication of feature variability and behavior solely due to inherent machine properties.

In a work by Valladares et al. [48] they have summarized several MRI (as well as CT and PET) texture analysis studies were the authors have tested different combinations of phantom materials for simulating tumor heterogeneity. Most phantoms are designed by embedding solid structures such as polystyrene spheres or porous

foams in an agarose gel mixture. However, the authors conclude that temperature and humidity regulations are limitations for using these phantoms as standard in multicenter trials. *Developing such a heterogeneous phantom (similar to the one by Rai et al.) for future feature stability research of a low-field integrated MRI-Linac would be an interesting expansion of the work in this thesis.*

Additional components to take into consideration is the segmentation and registration procedures. In this work identical cylindrical volumes placed in different regions of the two phantoms in the baseline set were propagated to the remaining imaging sets. Thus, the only uncertainty present is due to the registration. The ROIs were propagated via rigid registration since identical positioning for every scanning occasion was assumed and a phantom is considered an invariant object. All shape-based features were found to be stable in both phantoms, hence supporting the hypothesis of ideal imaging conditions. However, not all features within the long & short axis category (belonging to the shape-based features as well) were stable. This deviation is due to the choice of a cylindrical volume, which can have multiple options for long/short axis hence causing the feature value to vary randomly, rather than registration uncertainties.

For patient images an identical spherical volume was used for the liver data, but placed manually for every scanning occasion and not through rigid registration. The kidneys, however, were segmented manually one by one for every patient by a single user. This will affect the result due to intraobserver variability, any error will be systematic. Segmentation is, as mentioned in previous sections, a crucial part in the radiomics workflow chain and should be an uncertainty to take into account. Debates whether to seek ground truth or reproducibility are highly topical in present studies and different approaches are being investigated.

7 CONCLUSION

The stable features presented in table 2 are the result of quantitative image analysis on images from the scanner of a 0.35 T integrated MRI-Linac. Images were acquired with two different protocols; a high ($1.5mm^3$) and low ($1.5mm^2$ x 3mm) voxel resolution respectively. Two invariant objects, a basic phantom for daily QA and a more complex constructed phantom for monthly controls, represented ideal imaging conditions and were compared with patient data to identify common stable features. *Thus, this result indicates that there are radiomic features demonstrating robustness over a wide range of imaging conditions on a low-field integrated MRI-Linac, and that phantom studies can be useful for feature stability assessment. Additionally, it implies that the 0.35 T scanner in this study is sufficiently stable over time for performing radiomic studies.*

As mentioned in previous sections, features will be sensitive to image acquisition parameters, segmentation method etc to a certain extent. Assessing feature stability therefore ought to be a fundamental step in the radiomic process in order to formulate reliable predicative models, outcomes or conclusions. This study included analysis of 1087 radiomic features, of which 130 of them were found to be stable. As radiomics implies the throughput of a large amount of features, this result means that a relatively large number of features are robust and thereby appropriate for further outcome analysis or model building. On the other side, this also indicates that a many features are not appropriate for further clinical studies, emphasizing the value of stability assessment. Radiomic models need to be based on features with low variability that are insensitive to external factors. Hence, more research in this area is needed.

Although preliminary, these results are promising as several stable features also were found to have predictive value in different MRI-based radiomics papers. Radiomics has the potential to be an essential part in the pursuit of personalized oncology and this work provides a comprehensive investigation of radiomic features that can be used for future model building.

8 ACKNOWLEDGMENTS

I wish to express my deepest gratitude to my supervisor **Eduardo G. Moros** for his guidance and support throughout this project. Thank you for always taking the time to answer my questions, for being open to and coming with new ideas and for giving me the opportunity of a great learning experience overseas.

I would also like to thank **Geoffrey G. Zhang**, **Gage Redler**, **Kujtim Latifi** and **Vladimir Feygelman** from the Department of Radiation Oncology at Moffitt Cancer Center. Thank you for providing me with material and equipment, necessary information and helpful advise.

I wish to thank my supervisor guiding me from Sweden, **Crister Ceberg**. Thank you for your supervision, ideas, support and enthusiasm through this project.

Lastly, my sincere gratitude goes to my family and closest of friends for the never-ending support. Thank you to the West Wind Dojo, for giving me a sense of home in times of uncertainty.

References

[1] Socialstyrelsen Cancerfonden. Cancer i siffror 2018. Technical report, Cancerfonden, Socialstyrelsen, 2018.

[2] Cancer.Net. What is personalized cancer medicine?, January 2020.

[3] National Cancer Institute. Precision medicine in cancer treatment, October 2017.

[4] Sebastian Klüter. Technical design and concept of a 0.35 t mr-linac. *Clinical and Translational Radiation Oncology*, 2019.

[5] Yanle Hu, Leith Rankine, Olga L Green, Rojano Kashani, H Harold Li, Hua Li, Roger Nana, Vivian Rodriguez, Lakshmi Santanam, Shmaryu Shvartsman, James Victoria, H Omar Wooten, James F Dempsey, and Sasa Mutic. Characterization of the onboard imaging unit for the first clinical magnetic resonance image guided radiation therapy system. *Medical physics*, 42:5828–5837, October 2015.

[6] Robert J Gillies, Paul E Kinahan, and Hedvig Hricak. Radiomics: Images are more than pictures, they are data. *Radiology*, 278:563–577, February 2016.

[7] Philippe Lambin, Emmanuel Rios-Velazquez, Ralph Leijenaar, Sara Carvalho, Ruud G P M van Stiphout, Patrick Granton, Catharina M L Zegers, Robert Gillies, Ronald Boellard, André Dekker, and Hugo J W L Aerts. Radiomics: extracting more information from medical images using advanced feature analysis. *European journal of cancer (Oxford, England : 1990)*, 48:441–446, March 2012.

[8] Daniel L Saenz, Yue Yan, Neil Christensen, Margaret A Henzler, Lisa J Forrest, John E Bayouth, and Bhudatt R Paliwal. Characterization of a 0.35t mr system for phantom image quality stability and in vivo assessment of motion quantification. *Journal of applied clinical medical physics*, 16:30–40, November 2015.

[9] Sasa Mutic and James F Dempsey. The viewray system: magnetic resonance-guided and controlled radiotherapy. *Seminars in radiation oncology*, 24:196–199, July 2014.

[10] Alberto Traverso, Leonard Wee, Andre Dekker, and Robert Gillies. Repeatability and reproducibility of radiomic features: A systematic review. *International journal of radiation oncology, biology, physics*, 102:1143–1158, November 2018.

[11] Virendra Kumar, Yuhua Gu, Satrajit Basu, Anders Berglund, Steven A Eschrich, Matthew B Schabath, Kenneth Forster, Hugo J W L Aerts, Andre

Dekker, David Fenstermacher, Dmitry B Goldgof, Lawrence O Hall, Philippe Lambin, Yoganand Balagurunathan, Robert A Gatenby, and Robert J Gillies. Radiomics: the process and the challenges. *Magnetic resonance imaging*, 30:1234–1248, November 2012.

[12] Stefania Rizzo, Francesca Botta, Sara Raimondi, Daniela Origgi, Cristiana Fanciullo, Alessio Giuseppe Morganti, and Massimo Bellomi. Radiomics: the facts and the challenges of image analysis. *European radiology experimental*, 2:36, November 2018.

[13] Philippe Lambin, Ralph T H Leijenaar, Timo M Deist, Jurgen Peerlings, Evelyn E C de Jong, Janita van Timmeren, Sebastian Sanduleanu, Ruben T H M Larue, Aniek J G Even, Arthur Jochems, Yvonka van Wijk, Henry Woodruff, Johan van Soest, Tim Lustberg, Erik Roelofs, Wouter van Elmpt, Andre Dekker, Felix M Mottaghy, Joachim E Wildberger, and Sean Walsh. Radiomics: the bridge between medical imaging and personalized medicine. *Nature reviews. Clinical oncology*, 14:749–762, December 2017.

[14] Muhammad Shafiq-Ul-Hassan, Geoffrey G Zhang, Kujtim Latifi, Ghanim Ullah, Dylan C Hunt, Yoganand Balagurunathan, Mahmoud Abrahem Abdalah, Matthew B Schabath, Dmitry G Goldgof, Dennis Mackin, Laurence Edward Court, Robert James Gillies, and Eduardo Gerardo Moros. Intrinsic dependencies of ct radiomic features on voxel size and number of gray levels. *Medical physics*, 44:1050–1062, March 2017.

[15] Ke Nie, Hania Al-Hallaq, X Allen Li, Stanley H Benedict, Jason W Sohn, Jean M Moran, Yong Fan, Mi Huang, Michael V Knopp, Jeff M Michalski, James Monroe, Ceferino Obcemea, Christina I Tsien, Timothy Solberg, Jackie Wu, Ping Xia, Ying Xiao, and Issam El Naqa. Nctn assessment on current applications of radiomics in oncology. *International journal of radiation oncology, biology, physics*, 104:302–315, June 2019.

[16] Vishwa Parekh and Michael A Jacobs. Radiomics: a new application from established techniques. *Expert review of precision medicine and drug development*, 1:207–226, 2016.

[17] Alex Zwanenburg, Martin Vallières, Mahmoud A Abdalah, Hugo J W L Aerts, Vincent Andrearczyk, Aditya Apte, Saeed Ashrafinia, Spyridon Bakas, Roelof J Beukinga, Ronald Boellaard, Marta Bogowicz, Luca Boldrini, Irène Buvat, Gary J R Cook, Christos Davatzikos, Adrien Depeursinge, Marie-Charlotte Desseroit, Nicola Dinapoli, Cuong Viet Dinh, Sebastian Echegaray, Issam El Naqa, Andriy Y Fedorov, Roberto Gatta, Robert J Gillies, Vicky Goh, Michael Götz, Matthias Guckenberger, Sung Min Ha, Mathieu Hatt, Fabian

Isensee, Philippe Lambin, Stefan Leger, Ralph T H Leijenaar, Jacopo Lenkowicz, Fiona Lippert, Are Losnegård, Klaus H Maier-Hein, Olivier Morin, Henning Müller, Sandy Napel, Christophe Nioche, Fanny Orlhac, Sarthak Pati, Elisabeth A G Pfaehler, Arman Rahmim, Arvind U K Rao, Jonas Scherer, Muhammad Musib Siddique, Nanna M Sijtsema, Jairo Socarras Fernandez, Emiliano Spezi, Roel J H M Steenbakkers, Stephanie Tanadini-Lang, Daniela Thorwarth, Esther G C Troost, Taman Upadhaya, Vincenzo Valentini, Lisanne V van Dijk, Joost van Griethuysen, Floris H P van Velden, Philip Whybra, Christian Richter, and Steffen Löck. The image biomarker standardization initiative: Standardized quantitative radiomics for high-throughput image-based phenotyping. *Radiology*, page 191145, March 2020.

[18] Renee Cattell, Shenglan Chen, and Chuan Huang. Robustness of radiomic features in magnetic resonance imaging: review and a phantom study. *Visual Computing for Industry, Biomedicine, and Art*, 2(1):19, 2019.

[19] Alex Zwanenburg, Stefan Leger, Linda Agolli, Karoline Pilz, Esther G C Troost, Christian Richter, and Steffen Löck. Assessing robustness of radiomic features by image perturbation. *Scientific reports*, 9:614, January 2019.

[20] Robba Rai, Lois C Holloway, Carsten Brink, Matthew Field, Rasmus L Christiansen, Yu Sun, Michael B Barton, and Gary P Liney. Multicenter evaluation of mri-based radiomic features: A phantom study. *Medical physics*, April 2020.

[21] Terry K Koo and Mae Y Li. A guideline of selecting and reporting intraclass correlation coefficients for reliability research. *Journal of chiropractic medicine*, 15:155–163, June 2016.

[22] R. Kyle Padgett, Mariluz De Ornelas Couto, Tatiana Bejarano, and B. Ivaylo Mihaylov. Stability and variability of radiomcs features on a 0.35t mr-guided-rt system. Department of Radiation Oncology, University of Miami Miller School of Medicine, Miami, FL, USA.

[23] David Molina, Julián Pérez-Beteta, Alicia Martínez-González, Juan Martino, Carlos Velasquez, Estanislao Arana, and Víctor M Pérez-García. Lack of robustness of textural measures obtained from 3d brain tumor mris impose a need for standardization. *PloS one*, 12:e0178843, 2017.

[24] A Zwanenburg, S Leger, M Vallières, and S Löck. Image biomarker standardisation initiative. arxiv preprint arxiv: 161207003, 2019.

[25] Nailon Henry William. *Texture Analysis Methods for Medical Image Characterisation*. Biomedical Imaging, https://www.intechopen.com/books/biomedical-imaging/texture-analysis-methods-for-medical-image-characterisation, 2010.

[26] M. Robert Haralick, K. Shanmugam, and Dinstein Its'hak. Textural features for image classification. *IEEE Transactions on systems, man and cybernetics*, SMC-3(6), November 1973.

[27] Tommy Löfstedt, Patrik Brynolfsson, Thomas Asklund, Tufve Nyholm, and Anders Garpebring. Gray-level invariant haralick texture features. *PloS one*, 14:e0212110, 2019.

[28] Mary M Galloway. Texture analysis using grey level run lengths. *STIN*, 75:18555, 1974.

[29] Linda Shapiro and George Stockman. *Computer Vision*. The University of Washington and Department of Computer Science Michigan State University, 2000.

[30] M. T. Suzuki, Y. Yaginuma, T. Yamada, and Y. Shimizu. A shape feature extraction method based on 3D convolution masks. In *Proc. Eighth IEEE Int. Symp. Multimedia (ISM'06)*, pages 837–844, 2006.

[31] C Burrus Sidney, R Gopinath, and H Guo. Wavelets and wavelet transforms. *LaRecherche*, 1998.

[32] C Valens-A Really Friendly Guide. to wavelets. *C. Valens*, pages 4–16, 1999.

[33] Jiali Zhou, Jinghui Lu, Chen Gao, Jingjing Zeng, Changyu Zhou, Xiaobo Lai, Wenli Cai, and Maosheng Xu. Predicting the response to neoadjuvant chemotherapy for breast cancer: wavelet transforming radiomics in mri. *BMC cancer*, 20:100, February 2020.

[34] Davide Cusumano, Nicola Dinapoli, Luca Boldrini, Giuditta Chiloiro, Roberto Gatta, Carlotta Masciocchi, Jacopo Lenkowicz, Calogero Casà, Andrea Damiani, Luigi Azario, Johan Van Soest, Andre Dekker, Philippe Lambin, Marco De Spirito, and Vincenzo Valentini. Fractal-based radiomic approach to predict complete pathological response after chemo-radiotherapy in rectal cancer. *La Radiologia medica*, 123:286–295, April 2018.

[35] The Phanom Laboratory. *Magphan RT: MR imaging QA Designed for Radiotherapy*. The Phanom Laboratory.

[36] The Phantom Laboratory. *Magphan RT Phantom Manual*. The Phantom Laboratory, 2018.

[37] Kathryn E Mittauer, David AP Dunkerley, Poonam Yadav, and John E Bayouth. Characterization and longitudinal assessment of daily quality assurance for an mr-guided radiotherapy (mrgrt) linac. *Journal of Applied Clinical Medical Physics*, 20(11):27–36, 2019.

[38] Karen Buch, Hirofumi Kuno, Muhammad M Qureshi, Baojun Li, and Osamu Sakai. Quantitative variations in texture analysis features dependent on mri scanning parameters: A phantom model. *Journal of applied clinical medical physics*, 19:253–264, November 2018.

[39] Luca Boldrini, Davide Cusumano, Giuditta Chiloiro, Calogero Casà, Carlotta Masciocchi, Jacopo Lenkowicz, Francesco Cellini, Nicola Dinapoli, Luigi Azario, Stefania Teodoli, Maria Antonietta Gambacorta, Marco De Spirito, and Vincenzo Valentini. Delta radiomics for rectal cancer response prediction with hybrid 0.35 t magnetic resonance-guided radiotherapy (mrgrt): a hypothesis-generating study for an innovative personalized medicine approach. *La Radiologia medica*, 124:145–153, February 2019.

[40] Matthew B Spraker, Landon S Wootton, Daniel S Hippe, Kevin C Ball, Jan C Peeken, Meghan W Macomber, Tobias R Chapman, Michael N Hoff, Edward Y Kim, Seth M Pollack, Stephanie E Combs, and Matthew J Nyflot. Mri radiomic features are independently associated with overall survival in soft tissue sarcoma. *Advances in radiation oncology*, 4:413–421, 2019.

[41] Peter Gibbs and Lindsay W Turnbull. Textural analysis of contrast-enhanced mr images of the breast. *Magnetic Resonance in Medicine: An Official Journal of the International Society for Magnetic Resonance in Medicine*, 50(1):92–98, 2003.

[42] Teh-Chen Wang, Yan-Hao Huang, Chiun-Sheng Huang, Jeon-Hor Chen, Guei-Yu Huang, Yeun-Chung Chang, and Ruey-Feng Chang. Computer-aided diagnosis of breast dce-mri using pharmacokinetic model and 3-d morphology analysis. *Magnetic resonance imaging*, 32:197–205, April 2014.

[43] Ke Nie, Jeon-Hor Chen, Hon J Yu, Yong Chu, Orhan Nalcioglu, and Min-Ying Su. Quantitative analysis of lesion morphology and texture features for diagnostic prediction in breast mri. *Academic radiology*, 15:1513–1525, December 2008.

[44] Andreas Wibmer, Hedvig Hricak, Tatsuo Gondo, Kazuhiro Matsumoto, Harini Veeraraghavan, Duc Fehr, Junting Zheng, Debra Goldman, Chaya Moskowitz, Samson W Fine, Victor E Reuter, James Eastham, Evis Sala, and Hebert Alberto Vargas. Haralick texture analysis of prostate mri: utility for differentiating non-cancerous prostate from prostate cancer and differentiating prostate cancers with different gleason scores. *European radiology*, 25:2840–2850, October 2015.

[45] Emilie Niaf, Olivier Rouvière, Florence Mège-Lechevallier, Flavie Bratan, and Carole Lartizien. Computer-aided diagnosis of prostate cancer in the peripheral

zone using multiparametric mri. *Physics in medicine and biology*, 57:3833–3851, June 2012.

[46] Satish E Viswanath, Nicholas B Bloch, Jonathan C Chappelow, Robert Toth, Neil M Rofsky, Elizabeth M Genega, Robert E Lenkinski, and Anant Madabhushi. Central gland and peripheral zone prostate tumors have significantly different quantitative imaging signatures on 3 tesla endorectal, in vivo t2-weighted mr imagery. *Journal of magnetic resonance imaging : JMRI*, 36:213–224, July 2012.

[47] Maxime Lacroix, Frederique Frouin, Anne-Sophie Driand, Christophe Nioche, Fanny Orlhac, Jean-Francios Bernaudin, Pierre-Yves Brillet, and Irene Buvet. Correction for magnetic field inhomogeneities and normalization of voxel values are needed to better reveal the potential of mr radiomic features in lung cancer. *Front. Oncol.*, 2020.

[48] Alejandra Valladares, Thomas Beyer, and Ivo Rausch. Physical imaging phantoms for simulation of tumor heterogeneity in pet, ct, and mri: An overview of existing designs. *Medical physics*, 47:2023–2037, April 2020.

9 Appendix

Table 3: Robust radiomic features [%CoV mean value (standard deviation)] for the patient liver dataset.

Long & Short axis	**Intensity & Shaped based**	**LoG sigma=0.5mm**
LongAxis(mmCOM) [0.19 (0.09)]	V(voxels) [0.58 (0.23)]	Energy [0.72 (0.37)]
Maximum 3D diameter(mm) [0.13 (0.07)]	Volume [0.58 (0.23)]	Entropy [0.08 (0.04)]
	Surface area [0.73 (0.24)]	Hist entropy [1.95 (0.51)]
LoG sigma=1mm	Surface to volume ratio [0.32 (0.09)]	Norm energy [0.36 (0.28)]
Entropy [0.21 (0.10)]	Volume density(axis) [1.72 (0.89)]	Norm entropy [0.02 (0.02)]
Hist entropy [2.01 (0.87)]	Area density(axis) [1.23 (0.47)]	
Norm Entropy [0.15 (0.05)]	Volume density(convex) [0.58 (0.25)]	**LoG sigma=1.5mm**
	Area density (convex) [0.60 (0.27)]	Coeff vari [2.06 (1.66)]
LoG sigma=2mm	Sphericity [0.42 (0.09)]	Energy [1.88 (1.88)]
Coeff vari [3.03 (1.77)]	Asphericity [1.28 (0.28)]	Entropy [0.21 (0.08)]
Energy [2.45 (1.49)]	Compactness 1 [0.63 (0.14)]	Hist entropy [1.89 (0.79)]
Entropy [0.23 (0.12)]	Spherical disproportion [0.42 (0.09)]	Norm energy [1.55 (1.31)]
Hist entropy [1.86 (0.70)]	Volume fraction at 0.10 intensity [0.45 (0.26)]	Norm entropy [0.12 (0.09)]
Norm energy [2.31 (1.38)]	NIenergy [0.66 (0.35)]	
Norm entropy [0.17 (0.09)]	Entropy [0.08 (0.03)]	**LoG sigma=2.5mm**
	Hist entropy [2.26 (1.37)]	Coeff vari [3.90 (2.04)]
LoG sigma=3mm	Norm NIenergy [0.28 (0.23)]	Energy [3.22 (1.88)]
Coeff vari [4.33 (2.14)]	Norm entropy [0.02 (0.02)]	Entropy [0.30 (0.15)]
Energy [3.94 (2.40)]		Hist entropy [2.20 (0.81)]
Entropy [0.37 (0.21)]	**Wavelet LLL**	Norm energy [3.08 (1.77)]
Hist entropy [2.22 (0.84)]	Coeff vari [3.21 (1.21)]	Norm entropy [0.22 (0.13)]
Norm energy [3.52 (1.98)]	Energy [1.21 (0.59)]	
Norm entropy [0.27 (0.14)]	Entropy [0.14 (0.06)]	**Wavelet LLH**
	Hist entropy [1.27 (0.92)]	Coeff vari [3.70 (1.63)]
Wavelet LHL	Norm energy [1.39 (0.53)]	Entropy [0.69 (0.27)]
Entropy [1.41 (0.48)]	Norm entropy [0.13 (0.04)]	Hist entropy [1.15 (0.48)]
Hist entropy [1.12 (0.51)]		Norm entropy [0.70 (0.27)]
Norm entropy [1.40 (0.49)]		
	Wavelet HLL	**Wavelet LHH**
Wavelet HLH	Entropy [1.37 (0.58)]	Entropy [2.13 (0.88)]
Entropy [2.27 (1.02)]	Hist entropy [1.19 (0.33)]	Hist entropy [1.15 (0.48)]
Hist entropy [0.95 (0.50)]	Norm entropy [1.38 (0.59)]	Norm entropy [2.13 (0.91)]
Norm entropy [2.26 (1.02)]		
	Wavelet HHL	**Wavelet HHH**
Laws EEE	Entropy [1.55 (1.59)]	Coeff vari [3.90 (2.14)]
Hist entropy [1.71 (0.77)]	Hist entropy [1.13 (0.39)]	Energy [0.57 (0.27)]
		Entropy [0.07 (0.03)]
Laws EEL	**Laws EES**	Hist entropy [1.23 (0.43)]
Hist entropy [2.20 (1.09)]	Hist entropy [1.56 (0.67)]	Norm energy [0.23 (0.15)]
		Norm entropy [0.01 (0.01)]

Table 4: Robust radiomic features [%CoV mean value (standard deviation)] for the patient liver dataset.

Laws ELE	**Laws ELL**	
Hist entropy [1.83 (0.80)]	Hist entropy [2.16 (1.41)]	**Laws ELS**
		Hist entropy [1.84 (0.86)]
Laws ESE	**Laws ESL**	
Hist entropy [1.52 (0.35)]	Hist entropy [1.42 (0.66)]	**Laws ESS**
		Hist entropy [1.59 (0.62)]
Laws LEE	**Laws LEL**	
Hist entropy [1.86 (0.92)]	Hist entropy [1.81 (0.82)]	**Laws LES**
		Hist entropy [1.64 (0.81)]
Laws LLE	**Laws LLL**	
Hist entropy [1.96 (0.87)]	Energy [0.66 (0.33)]	**Laws LLS**
	Entropy [0.08 (0.03)]	Hist entropy [2.09 (1.03)]
Laws LSE	Hist entropy [2.71 (1.28)]	
Hist entropy [1.90 (0.70)]	Norm energy [0.23 (0.24)]	**Laws LSL**
	Norm entropy [0.02 (0.02)]	Hist entropy [2.79 (1.41)]
Laws LSS		
Hist entropy [1.78 (0.68)]	**Laws SEE**	**Laws SEL**
	Hist entropy [1.33 (0.73)]	Hist entropy [1.71 (0.89)]
Laws SES		
Hist entropy [1.63 (0.94)]	**Laws SLE**	**Laws SLL**
	Hist entropy [1.76 (0.76)]	Hist entropy [2.49 (1.49)]
Laws SLS		
Hist entropy [1.61 (0.68)]	**Laws SSE**	**Laws SSL**
	Hist entropy [1.38 (0.41)]	Hist entropy [1.23 (0.26)]
Laws SSS		
Hist entropy [1.70 (0.64)]	**Co-occurrence**	**Run-length**
	Entropy [3.46 (1.38)]	SRE [0.91 (0.59)]
Gray-level size-zone	Mean [1.01 (0.48)]	LRE [3.59 (2.32)]
-	Inverse diff. moment [0.35 (0.13)]	RLNU [3.58 (1.96)]
	Inverse diff. [0.93 (0.37)]	RPC [1.38 (0.66)]
Neigborhood Gray-Tone Diff.	Sum entropy [3.42 (1.39)]	
-	Vnorm Mean [0.70(0.42)]	**Fractal dimension**
	Gnorm Entropy [3.46 (1.38)]	meanLac1 [3.81 (2.42)]
	Gnorm Sum Entropy [3.42 (1.39)]	meanLac2 [1.10 (0.66)]
	Gnorm Mean [1.01 (0.48)]	meanLac3 [0.60 (0.22)]
	VGnorm Mean [0.70 (0.42)]	

Table 5: Robust radiomic features [%CoV mean value (standard deviation)] for the patient kidney dataset.

Long & Short axis	**Intensity & Shaped based**	**LoG sigma=0.5mm**
LongAxis(mmCOM) [1.60 (0.61)]	V(voxels) [2.41 (0.87)]	Energy [2.71 (0.93)]
Maximum 3D diameter(mm) [1.19 (0.50)]	Volume [2.41 (0.87)]	Entropy [0.25 (0.09)]
	Surface area [1.64 (0.70)]	Hist entropy [1.90 (0.47)]
LoG sigma=1mm	Surface to volume ratio [1.49 (0.54)]	Norm energy [0.65 (0.35)]
Entropy [0.29 (0.10)]	Volume density(axis) [3.25 (1.15)]	Norm entropy [0.03 (0.02)]
Hist entropy [1.85 (0.92)]	Area density(axis) [1.80 (0.43)]	
Norm Entropy [0.06 (0.03)]	Volume density(convex) [0.79 (0.33)]	**LoG sigma=1.5mm**
	Area density (convex) [0.72 (0.37)]	Coeff vari [1.28 (0.58)]
LoG sigma=2mm	Sphericity [1.04 (0.41)]	Energy [2.92 (1.08)]
Coeff vari [1.68 (0.80)]	Asphericity [2.31 (0.87)]	Entropy [0.29 (0.11)]
Energy [3.17 (1.06)]	Compactness 1 [1.56 (0.62)]	Hist entropy [1.79 (0.74)]
Entropy [0.30 (0.11)]	Spherical disproportion [1.05 (0.41)]	Norm energy [1.01 (0.46)]
Hist entropy [2.00 (0.90)]	Volume fraction at 0.10 intensity [0.57 (0.53)]	Norm entropy [0.06 (0.02)]
Norm energy [1.36 (0.66)]	NIenergy [2.71 (0.98)]	
Norm entropy [0.08 (0.03)]	Entropy [0.25 (0.09)]	**LoG sigma=2.5mm**
	Hist entropy [1.21 (0.47)]	Coeff vari [2.08 (1.12)]
LoG sigma=3mm	Norm NIenergy [0.61 (0.35)]	Energy [3.45 (1.13)]
Coeff vari [2.10 (1.17)]	Norm entropy [0.03 (0.02)]	Entropy [0.31 (0.11)]
Energy [3.56 (1.33)]		Hist entropy [2.02 (1.13)]
Entropy [0.32 (0.13)]	**Wavelet LLL**	Norm energy [1.76 (0.98)]
Hist entropy [2.00 (1.03)]	Coeff vari [3.08 (1.39)]	Norm entropy [0.10 (0.0.4)]
Norm energy [1.82 (1.04)]	Energy [3.06 (1.23)]	
Norm entropy [0.10 (0.05)]	Entropy [0.28 (0.12)]	**Wavelet LLH**
	Hist entropy [1.12 (0.38)]	Coeff vari [4.55 (1.89)]
Wavelet LHL	Norm energy [1.63 (0.70)]	Entropy [1.13 (0.51)]
Entropy [0.99 (0.44)]	Norm entropy [0.12 (0.06)]	Hist entropy [1.40 (0.52)]
Hist entropy [1.62 (0.60)]		Norm entropy [1.13 (0.50)]
Norm entropy [0.96 (0.45)]		
	Wavelet HLL	**Wavelet LHH**
Wavelet HLH	Entropy [1.16 (0.70)]	Entropy [2.28 (1.01)]
Entropy [3.07 (1.08)]	Hist entropy [1.24 (0.56)]	Hist entropy [1.46 (0.62)]
Hist entropy [2.13 (0.79)]	Norm entropy [2.24 (0.99)]	Norm entropy [2.13 (0.91)]
Norm entropy [3.08 (1.12)]		
	Wavelet HHL	**Wavelet HHH**
Laws EEE	Entropy [2.98 (1.40)]	Coeff vari [4.66 (2.59)]
Hist entropy [1.33 (0.65)]	Hist entropy [1.22 (0.40)]	Energy [2.64 (1.02)]
		Entropy [0.24 (0.09)]
Laws EEL	**Laws EES**	Hist entropy [1.18 (0.46)]
Hist entropy [1.54 (0.77)]	Hist entropy [1.23 (0.58)]	Norm energy [0.47 (0.28)]
		Norm entropy [0.02 (0.01)]

Table 6: Robust radiomic features [%CoV mean value (standard deviation)] for the patient kidney dataset.

Laws ELE	**Laws ELL**	
Hist entropy [1.45 (0.62)]	Hist entropy [1.41 (0.69)]	**Laws ELS**
		Hist entropy [1.69 (0.54)]
Laws ESE	**Laws ESL**	
Hist entropy [1.40 (0.80)]	Hist entropy [1.97 (1.01)]	**Laws ESS**
		Hist entropy [1.29 (0.60)]
Laws LEE	**Laws LEL**	
Hist entropy [1.82 (0.94)]	Hist entropy [1.82 (0.62)]	**Laws LES**
		Hist entropy [1.74 (0.96)]
Laws LLE	**Laws LLL**	
Hist entropy [1.76 (0.68)]	Energy [2.69 (0.88)]	**Laws LLS**
	Entropy [0.25 (0.09)]	Hist entropy [2.48 (1.17)]
Laws LSE	Hist entropy [1.32 (0.70)]	
Hist entropy [1.91 (1.11)]	Norm energy [0.53 (0.35)]	**Laws LSL**
	Norm entropy [0.02 (0.02)]	Hist entropy [2.19 (0.82)]
Laws LSS		
Hist entropy [1.73 (0.76)]	**Laws SEE**	**Laws SEL**
	Hist entropy [1.11 (0.35)]	Hist entropy [1.17 (0.55)]
Laws SES		
Hist entropy [1.47 (0.58)]	**Laws SLE**	**Laws SLL**
	Hist entropy [1.44 (0.59)]	Hist entropy [1.66 (0.69)]
Laws SLS		
Hist entropy [1.33 (0.49)]	**Laws SSE**	**Laws SSL**
	Hist entropy [1.51 (0.81)]	Hist entropy [1.98 (0.86)]
Laws SSS		
Hist entropy [1.49 (0.49)]	**Co-occurrence**	**Run-length**
	Entropy [1.72 (0.80)]	SRE 3.45 (1.81)]
Gray-level size-zone	Mean [2.71 (0.85)]	LRE [3.45 (1.81)]
-	Inverse diff. moment [0.08 (0.04)]	RLNU [4.17 (1.70)]
	Inverse diff. [0.31 (0.15)]	RPC [1.19 (0.62)]
Neigborhood Gray-Tone Diff.	Sum entropy [1.73 (0.80)]	
-	Vnorm Mean [0.63 (0.32)]	**Fractal dimension**
	Gnorm Entropy [1.72 (0.80)]	meanLac1 [4.36 (1.92)]
	Gnorm Sum Entropy [1.73 (0.80)]	meanLac2 [1.25 (0.49)]
	Gnorm Mean [2.71 (0.85)]	meanLac3 [2.00 (0.72)]
	VGnorm Mean [0.63 (0.32)]	

Table 7: Robust radiomic features [%CoV mean value (standard deviation)] for the Magphan® RT phantom dataset.

Long & Short axis	**Intensity & Shaped based**	**LoG sigma=0.5mm**
LongAxis(mmCOM) [0.45 (0.16)]	V(voxels) [1.37 (0.99)]	Energy [2.15 (0.72)]
Maximum 3D diameter(mm) [0.37 (0.14)]	Volume [1.37 (0.99)]	Entropy [0.45 (0.08)]
	Surface area [0.58 (0.07)]	Hist entropy [1.01 (0.25)]
LoG sigma=1mm	Surface to volume ratio [1.19 (1.05)]	Norm energy [1.97 (0.27)]
Entropy [0.50 (0.09)]	Volume density(axis) [3.83 (3.43)]	Norm entropy [0.27 (0.06)]
Hist entropy [2.63 (0.84)]	Area density(axis) [1.51 (0.80)]	
Norm Entropy [0.34 (0.12)]	Volume density(convex) [1.02 (0.70)]	**LoG sigma=1.5mm**
	Area density (convex) [0.40 (0.23)]	Coeff vari [2.94 (0.80)]
LoG sigma=2mm	Sphericity [0.80 (0.61)]	Energy [3.00 (0.98)]
Coeff vari [2.30 (0.37)]	Asphericity [1.97 (1.53)]	Entropy [0.39 (0.10)]
Energy [2.44 (0.80)]	Compactness 1 [1.20 (0.91)]	Hist entropy [1.93 (0.18)]
Entropy [0.35 (0.16)]	Spherical disproportion [0.82 (0.64)]	Norm energy [0.33 (0.13)]
Hist entropy [1.08 (0.09)]	Volume fraction at 0.10 intensity [2.88 (2.24)]	Norm entropy [0.06 (0.02)]
Norm energy [2.12 (0.21)]	NIenergy [2.24 (0.61)]	
Norm entropy [0.22 (0.05)]	Entropy [0.35 (0.06)]	**LoG sigma=2.5mm**
	Hist entropy [1.59 (0.65)]	Coeff vari [3.77 (0.86)]
LoG sigma=3mm	Norm NIenergy [1.25 (0.71)]	Energy 3.86 (1.34)]
Coeff vari [4.28 (0.81)]	Norm entropy [0.21 (0.11)]	Entropy [0.53 (0.19)]
Energy [4.60 (1.58)]		Hist entropy [1.43 (0.57)]
Entropy [0.62 (0.22)]	**Wavelet LLL**	Norm energy [3.26 (0.63)]
Hist entropy [1.19 (0.31)]	Coeff vari [2.59 (0.90)]	Norm entropy [0.39 (0.12)]
Norm energy [3.72 (0.90)]	Energy [2.08 (0.38)]	
Norm entropy [0.45 (0.14)]	Entropy [0.27 (0.05)]	**Wavelet LLH**
	Hist entropy [1.30 (0.55)]	Coeff vari [3.34 (1.74)]
Wavelet LHL	Norm energy [1.82 (0.72)]	Entropy [0.78 (0.52)]
Entropy [1.17 (0.63)]	Norm entropy [0.22 (0.09)]	Hist entropy [0.49 (0.19)]
Hist entropy [0.49 (0.02)]		Norm entropy [0.79 (0.66)]
Norm entropy [1.11 (0.53)]		
	Wavelet HLL	**Wavelet LHH**
Wavelet HLH	Entropy [1.24 (1.36)]	Entropy [3.24 (2.95)]
Entropy [3.09 (1.65)]	Hist entropy [0.59 (0.26)]	Hist entropy [0.41 (0.12)]
Hist entropy [0.52 (0.20)]	Norm entropy [1.21 (1.24)]	Norm entropy [3.26 (2.90)]
Norm entropy [3.04 (1.69)]		
	Wavelet HHL	**Wavelet HHH**
Laws EEE	Entropy [4.99 (6.74)]	Coeff vari [2.59 (1.13)]
Hist entropy [1.59 (0.63)]	Hist entropy [0.57 (0.17)]	Energy [1.88 (0.78)]
		Entropy [0.24 (0.11)]
Laws EEL	**Laws EES**	Hist entropy [0.58 (0.17)]
Hist entropy [1.68 (0.38)]	Hist entropy [2.40 (1.02)]	Norm energy [0.97 (0.55)]
		Norm entropy [0.11 (0.06)]

Table 8: Robust radiomic features [%CoV mean value (standard deviation)] for the Magphan® RT phantom dataset.

Laws ELE	**Laws ELL**	
Hist entropy [1.71 (1.25)]	Hist entropy [1.69 (0.69)]	**Laws ELS**
		Hist entropy [1.38 (0.26)]
Laws ESE	**Laws ESL**	
Hist entropy [1.79 (0.20)]	Hist entropy [2.48 (1.10)]	**Laws ESS**
		Hist entropy [2.55 (0.83)]
Laws LEE	**Laws LEL**	
Hist entropy [1.58 (0.44)]	Hist entropy [1.24 (0.35)]	**Laws LES**
		Hist entropy [1.53 (0.21)]
Laws LLE	**Laws LLL**	
Hist entropy [1.66 (0.73)]	Energy [2.20 (0.67)]	**Laws LLS**
	Entropy [0.30 (0.09)]	Hist entropy [1.31 (0.46)]
Laws LSE	Hist entropy [0.82 (0.32)]	
Hist entropy [1.82 (0.68)]	Norm energy [1.10 (0.81)]	**Laws LSL**
	Norm entropy [0.15 (0.10)]	Hist entropy [3.16 (1.12)]
Laws LSS		
Hist entropy [2.62 (1.02)]	**Laws SEE**	**Laws SEL**
	Hist entropy [2.01 (0.38)]	Hist entropy [1.88 (0.34)]
Laws SES		
Hist entropy [2.26 (1.30)]	**Laws SLE**	**Laws SLL**
	Hist entropy [1.40 (0.51)]	Hist entropy [1.79 (0.36)]
Laws SLS		
Hist entropy [2.46 (1.05)]	**Laws SSE**	**Laws SSL**
	Hist entropy [2.57 (0.88)]	Hist entropy [2.66 (0.42)]
Laws SSS		
Hist entropy [2.75 (0.18)]	**Co-occurrence**	**Run-length**
	Entropy [1.59 (0.29)]	SRE [0.85 (0.24)]
Gray-level size-zone	Mean [1.86 (0.91)]	LRE [3.30 (1.57)]
-	Inverse diff. moment [0.17 (0.10)]	RLNU [4.61 (1.35)]
	Inverse diff. [0.24 (0.07)]	RPC [3.16 (1.25)]
Neigborhood Gray-Tone Diff.	Sum entropy [1.55 (0.52)]	
-	Vnorm Mean [0.96 (0.32)]	**Fractal dimension**
	Gnorm Entropy [1.59 (0.29)]	meanLac1 [2.34 (0.62)]
	Gnorm Sum Entropy [1.55 (0.52)]	meanLac2 [1.85 (1.20)]
	Gnorm Mean [1.86 (0.91)]	meanLac3 [1.06 (0.49)]
	VGnorm Mean [0.96 (0.32)]	

Table 9: Robust radiomic features [%CoV mean value (standard deviation)] for the ViewRay Daily QA phantom dataset.

Long & Short axis	**Intensity & Shaped based**	**LoG sigma=0.5mm**
LongAxis(mmCOM) [0.47 (0.01)]	V(voxels) [0.55 (0.18)]	Energy [0.75 (0.26)]
Maximum 3D diameter(mm) [0.50 (0.09)]	Volume [0.55 (0.18)]	Entropy [0.10 (0.04)]
	Surface area [0.52 (0.07)]	Hist entropy [1.41 (0.18)]
LoG sigma=1mm	Surface to volume ratio [0.22 (0.10)]	Norm energy [0.46 (0.13)]
Entropy [0.58 (0.21)]	Volume density(axis) [1.30 (0.93)]	Norm entropy [0.05 (0.02)]
Hist entropy [3.45 (0.66)]	Area density(axis) [0.95 (0.70)]	
Norm Entropy [0.49 (0.19)]	Volume density(convex) [0.50 (0.16)]	**LoG sigma=1.5mm**
	Area density (convex) [0.32 (0.08)]	Coeff vari [3.01 (0.58)]
LoG sigma=2mm	Sphericity [0.20 (0.20)]	Energy [3.01 (0.78)]
Coeff vari [3.71 (0.31)]	Asphericity [0.48 (0.47)]	Entropy [0.35 (0.09)]
Energy [2.86 (0.58)]	Compactness 1 [0.30 (0.30)]	Hist entropy [2.17 (0.59)]
Entropy [0.29 (0.04)]	Spherical disproportion [0.20 (0.20)]	Norm energy [2.34 (0.54)]
Hist entropy [1.84 (0.34)]	Volume fraction at 0.10 intensity [0.30 (0.07)]	Norm entropy [0.22 (0.05)]
Norm energy [2.96 (0.37)]	NIenergy [0.72 (0.26)]	
Norm entropy [0.29 (0.02)]	Entropy [0.10 (0.04)]	**LoG sigma=2.5mm**
	Hist entropy [1.84 (0.70)]	Coeff vari [4.29 (0.12)]
LoG sigma=3mm	Norm NIenergy [0.20 (0.08)]	Energy [3.83 (0.48)]
Coeff vari [3.41 (0.83)]	Norm entropy [0.03 (0.01)]	Entropy [0.46 (0.08)]
Energy [3.91 (0.27)]		Hist entropy [2.33 (0.34)]
Entropy [0.51 (0.04)]	**Wavelet LLL**	Norm energy [3.44 (0.07)]
Hist entropy [1.77 (0.11)]	Coeff vari [1.74 (0.62)]	Norm entropy [0.33 (0.03)]
Norm energy [2.72 (0.87)]	Energy [1.33 (0.56)]	
Norm entropy [0.27 (0.07)]	Entropy [0.16 (0.06)]	**Wavelet LLH**
	Hist entropy [0.95 (0.41)]	Coeff vari [2.62 (0.89)]
Wavelet LHL	Norm energy [1.04 (0.39)]	Entropy [0.37 (0.15)]
Entropy [0.78 (0.51)]	Norm entropy [0.11 (0.04)]	Hist entropy [0.60 (0.16)]
Hist entropy [0.54 (0.06)]		Norm entropy [0.79 (0.66)]
Norm entropy [0.76 (0.48)]		
	Wavelet HLL	**Wavelet LHH**
Wavelet HLH	Entropy [0.53 (0.34)]	Entropy [1.49 (0.34)]
Entropy [3.24 (2.42)]	Hist entropy [0.66 (0.24)]	Hist entropy [0.46 (0.16)]
Hist entropy [0.58 (0.25)]	Norm entropy [0.56 (0.37)]	Norm entropy [1.51 (0.32)]
Norm entropy [3.22 (2.39)]		
	Wavelet HHL	**Wavelet HHH**
Laws EEE	Entropy [0.83 (0.25)]	Coeff vari [1.91 (1.26)]
Hist entropy [2.44 (0.69)]	Hist entropy [0.54 (0.19)]	Energy [1.80 (0.42)]
		Entropy [0.10 (0.04)]
Laws EEL	**Laws EES**	Hist entropy [0.37 (0.02)]
Hist entropy [3.04 (0.78)]	Hist entropy [2.92 (0.83)]	Norm energy [0.41 (0.27)]
		Norm entropy [0.03 (0.02)]

Table 10: Robust radiomic features [%CoV mean value (standard deviation)] for the ViewRay Daily QA phantom dataset.

Laws ELE	**Laws ELL**	
Hist entropy [2.93 (0.35)]	Hist entropy [1.98 (0.18)]	**Laws ELS**
		Hist entropy [2.63 (0.29)]
Laws ESE	**Laws ESL**	
Hist entropy [2.81 (0.64)]	Hist entropy [3.01 (1.69)]	**Laws ESS**
		Hist entropy [2.59 (1.02)]
Laws LEE	**Laws LEL**	
Hist entropy [0.83 (0.33)]	Hist entropy [1.21 (0.07)]	**Laws LES**
		Hist entropy [1.25 (0.01)]
Laws LLE	**Laws LLL**	
Hist entropy [0.82 (0.10)]	Energy [0.70 (0.26)]	**Laws LLS**
	Entropy [0.10 (0.04)]	Hist entropy [0.71 (0.34)]
Laws LSE	Hist entropy [2.15 (1.12)]	
Hist entropy [1.34 (0.03)]	Norm energy [0.19 (0.06)]	**Laws LSL**
	Norm entropy [0.03 (0.01)]	Hist entropy [1.57 (0.39)]
Laws LSS		
Hist entropy [1.60 (0.01)]	**Laws SEE**	**Laws SEL**
	Hist entropy [2.53 (0.19)]	Hist entropy [2.68 (0.31)]
Laws SES		
Hist entropy [2.94 (0.04)]	**Laws SLE**	**Laws SLL**
	Hist entropy [3.08 (0.78)]	Hist entropy [2.49 (0.08)]
Laws SLS		
Hist entropy [3.35 (0.46)]	**Laws SSE**	**Laws SSL**
	Hist entropy [3.32 (0.66)]	Hist entropy [3.15 (0.20)]
Laws SSS		
Hist entropy [3.56 (0.44)]	**Co-occurrence**	**Run-length**
	Entropy [2.13 (0.58)]	SRE [0.55 (0.16)]
Gray-level size-zone	Mean [1.02 (0.10)]	LRE [2.33 (1.01)]
-	Inverse diff. moment [0.07 (0.03)]	RLNU [3.18 (0.61)]
	Inverse diff. [0.11 (0.01)]	RPC [2.13 (0.25)]
Neigborhood Gray-Tone Diff.	Sum entropy [2.24 (0.38)]	
-	Vnorm Mean [0.77 (0.21)]	**Fractal dimension**
	Gnorm Entropy [2.13 (0.58)]	meanLac1 [0.68 (0.07)]
	Gnorm Sum Entropy [2.24 (0.38)]	meanLac2 [0.92 (0.25)]
	Gnorm Mean [1.02 (0.10)]	meanLac3 [0.78 (0.14)]
	VGnorm Mean [0.77 (0.22)]	